Geophysical Journal International

Geophys. J. Int. (2015) **202,** 277–297
GJI Geodynamics and tectonics

doi: 10.1093/gji/ggv127

Fluid budgets along the northern Hikurangi subduction margin, New Zealand: the effect of a subducting seamount on fluid pressure

Susan Ellis,[1] Åke Fagereng,[2] Dan Barker,[1] Stuart Henrys,[1] Demian Saffer,[3] Laura Wallace,[4] Charles Williams[1] and Rob Harris[5]

[1] *GNS Science, PO Box* 30-368, *Avalon, Lower Hutt* 5010, *New Zealand. E-mail: s.ellis@gns.cri.nz*
[2] *Department of Geological Sciences, University of Cape Town, Rondebosch* 7701, *South Africa; now at Cardiff University, Park Place, Cardiff CF*10 3*AT, United Kingdom*
[3] *Department of Geosciences, Penn State,* 534 *Deike Building, University Park, PA* 16802, *USA*
[4] *Institute for Geophysics, J.J. Pickle Research Campus, Bldg.* 196, 10100 *Burnet Rd. (R*2200*), Austin, TX* 78758-4445, *USA*
[5] *College of Earth, Ocean, and Atmospheric Sciences, Oregon State University,* 104 *CEOAS Admin Bldg, Corvallis OR* 97331-5503, *USA*

Accepted 2015 March 12. Received 2015 January 21; in original form 2014 July 16

SUMMARY

We estimate fluid sources around a subducted seamount along the northern Hikurangi subduction margin of New Zealand, using thermomechanical numerical modelling informed by wedge structure and porosities from multichannel seismic data. Calculated fluid sources are input into an independent fluid-flow model to explore the key controls on overpressure generation to depths of 12 km. In the thermomechanical models, sediment transport through and beneath the wedge is calculated assuming a pressure-sensitive frictional rheology. The change in porosity, pressure and temperature with calculated rock advection is used to compute fluid release from compaction and dehydration. Our calculations yield more precise information about source locations in time and space than previous averaged estimates for the Hikurangi margin. The volume of fluid release in the wedge is smaller than previously estimated from margin-averaged calculations ($\sim$14 m^3 yr^{-1} m^{-1}), and is exceeded by fluid release from underlying (subducting) sediment ($\sim$16 m^3 yr^{-1} m^{-1}). Clay dehydration contributes only a small quantity of fluid by volume ($\sim$2 m^3 yr^{-1} m^{-1} from subducted sediment), but the integrated effect is still significant landward of the seamount. Fluid source terms are used to estimate fluid pressures around a subducting seamount in the fluid-flow models, using subducted sediment permeability derived from porosity, and testing two end-members for décollement permeability. Models in which the décollement acts as a fluid conduit predict only moderate fluid overpressure in the wedge and subducting sediment. However, if the subduction interface becomes impermeable with depth, significant fluid overpressure develops in subducting sediment landward of the seamount. The location of predicted fluid overpressure and associated dehydration reactions is consistent with the idea that short duration, shallow, slow slip events (SSEs) landward of the seamount are caused by anomalous fluid pressures; alternatively, it may result from frictional effects of changing clay content along the subduction interface.

Key words: Fault zone rheology; Rheology and friction of fault zones; Subduction zone processes; Continental margins: convergent; High strain deformation zones; New Zealand.

1 INTRODUCTION

Fluids are thought to critically modulate frictional properties and sediment deformation at convergent plate boundaries. Fluid pressures approaching lithostatic values have been proposed to explain transient slow slip behaviour along subduction interfaces by locally lowering effective normal stresses (e.g. Kodaira *et al.* 2004; Liu & Rice 2005, 2007; Kitajima & Saffer 2012; Bassett *et al.* 2014), while over longer time spans, fluid pressures are a dominant control on fault and sediment strength, and thus on wedge morphology and the manner by which sediments are incorporated into an accretionary wedge or subducted to depth (e.g. Davis *et al.* 1983; Dahlen 1984, 1990; Dahlen *et al.* 1984; Matmon & Bekins 2006; Saffer & Bekins 2006). Through these mechanisms, fluid flow and the distribution of elevated fluid pressure can influence the seismic hazard at subduction zones.

Understanding how fluid pressure affects subduction dynamics requires determination of fluid release, pathways and flow-rates

at depth. Studies of current and ancient accretionary prisms show that fluid pressure must locally reach near-lithostatic values as documented by tensile quartz and carbonate veins in exhumed rocks, active fluid vents and near-surface fluid pressures measured in wells (e.g. Byrne & Fisher 1990; Becker *et al.* 1997; Saffer 2003). However, the temporal and spatial extent of such overpressured zones throughout the plate boundary system is not as well defined. Attempts have been made to estimate fluid sources and sinks within accretionary wedges using wedge bathymetry, information on porosities derived from seismic data, and calculations of the release of clay-bound fluids due to increasing pressure and temperature as sediment is transported to depth (e.g. Bray & Karig 1985; Screaton *et al.* 1990; Bekins & Dreiss 1992; Wang 1994; Saffer & Bekins 1998; Skarbek & Saffer 2009; Moore *et al.* 2011). Such calculations can be partially informed by deep drilling projects (e.g. Moore *et al.* 2001; Tobin & Kinoshita 2006). Overall though, many assumptions must be made to relate geological and geophysical estimates of fluid pressure along the subduction interface to the change in total fluid inventory and dewatering rates through time as material enters and passes through the wedge or underlying layers.

In this paper, we outline a method to combine mechanical models of sediment accretion and subduction with rock physical properties derived from detailed seismic sections, in order to estimate fluid release (fluid sources) along a subduction margin. We apply this technique to the northern Hikurangi subduction margin, offshore North Island, New Zealand. This region has recently been the focus of international efforts to understand transient (slow) slip events at subduction margins. Subduction of a seamount and excess pore fluid pressures along and above the subduction interface there have been implicated in the particularly shallow region over which slow-slip events (SSEs) have been observed (e.g. Wallace *et al.* 2009; Wallace & Beavan 2010; Fig. 1). We attempt to predict likely fluid pressure variations with depth in order to help inform such observations. We include interface geometry and porosity data based on seismic profiles to consider the effect of fluid generation at depth caused by compaction of incoming sediments, to answer the following questions:

(1) Given margin geometry, porosity, fluid sources and estimated permeabilities for the northern Hikurangi margin, is fluid overpressure possible and if so, what is the spatial distribution of overpressure?

(2) What is the influence of seamount subduction on development of overpressure?

(3) Does fluid overpressure (if present) correlate spatially with areas of slow slip and other geophysical anomalies?

2 BACKGROUND AND GEOLOGICAL SETTING OF THE NORTHERN HIKURANGI SUBDUCTION MARGIN

The Pacific Plate subducts obliquely beneath the eastern North Island, New Zealand, along the Hikurangi trench at 4.5–5.5 cm yr^{-1} (Wallace *et al.* 2004; Fig. 1). The lower plate consists of anomalously thick (>15 km) oceanic crust of the Hikurangi Plateau (Davy & Wood 1994; Mortimer & Parkinson 1996; Davy *et al.* 2008). Numerous seamounts are interpreted impinging on the northern part of the subduction zone offshore of Gisborne (Fig. 1), and subducted seamounts have also been inferred from seismic profiles, magnetic anomalies and large-scale embayments within the upper plate (Collot *et al.* 2001; Pedley *et al.* 2010). In contrast to the broad (>100 km) accretionary margin farther south, the northern portion of the Hikurangi margin is relatively sediment-starved with a narrow, frontal zone of imbricate thrusts (Lewis *et al.* 1998; Barker *et al.* 2009), a steep (∼8° dip near the toe) seafloor slope, and evidence of frontal subduction erosion associated with subducting seamounts (e.g. Collot *et al.* 1996, 2001). Seismic reflection profiles in this region show a thin (on average ∼1–2 km thick) Cenozoic to Mesozoic sedimentary cover on the incoming plate (Barker *et al.* 2009). This is composed of a horizontal succession of Mesozoic volcaniclastic sediments, overlain by a condensed Late Cretaceous-Early Oligocene sequence of nannofossil chalks alternating with mudstones, and *ca*. 1-km-thick succession of Cretaceous hemipelagic and trench-fill sediments (Davy & Wood 1994; Davy *et al.* 2008; Barnes *et al.* 2010; Pedley *et al.* 2010). In addition, up to *ca*. 3 km of older Cretaceous volcaniclastics and limestone/chert comprise the top of the basaltic Hikurangi Plateau (Davy *et al.* 2008). The condensed Cretaceous/Paleogene sequence is important for this study since the subducting plate interface develops at or close to the top of this sequence (Plaza-Faverola *et al.* 2012).

The northern margin offshore Gisborne has been classified as an episodically erosional convergent margin, owing to the oversteepened frontal slope, presence of subducting seamounts, and episodes of frontal tectonic erosion preserved in trench and wedge morphology. These are evident from several prominent indentations and extensive regions of gravitational collapse within the inboard trench slope (Collot *et al.* 1996; Barker *et al.* 2009; Pedley *et al.* 2010). The narrow frontal wedge abuts a backstop of Mesozoic greywacke, an inner, highly deformed pre-subduction Cretaceous and Paleogene sequence covered with deformed Miocene-Recent basins, and an outer accretionary wedge composed of mainly Plio-Pleistocene turbidites (Lewis & Pettinga 1993; Lewis *et al.* 1998; Barnes *et al.* 2010). Structural analyses indicate that up to 90 per cent of the total regional convergence is absorbed between the coast and the deformation front; the inactivity of the upper slope and mid-slope regions suggests that most of this deformation is currently occurring within the frontal accretionary wedge across the up-dip extent of the interplate thrust, that is in the outermost 2–3 thrust slices, <10 km from the trench (Pedley *et al.* 2010; Bell, unpublished data). This frontal region may therefore be considered to be presently accretive rather than erosive.

The northern Hikurangi margin has a shallow transition from interseismically locked to aseismically creeping behaviour (<5–15 km) that coincides spatially with well-characterized SSEs that last 2–3 weeks and occur every 1–2 yr (Wallace & Beavan 2010; Wallace *et al.* 2012; Fig. 1). Multichannel seismic data reveal regions where the interface (between <5 km to >10–16 km depth) follows the top of a thick high-amplitude reflectivity zone ('HRZ') that coincides with the source areas of some SSEs (Fig. 1). Bell *et al.* 2010 suggested that the high-amplitude reflectivity may be the result of high fluid concentrations within sediments, entrained between downgoing seamounts. If this interpretation is correct, then the correlation between HRZ and SSEs would suggest that fluids exert an important control on the generation of slow slip (Kitajima & Saffer 2012; Bassett *et al.* 2014). Alternatively, the SSEs could be related to lithological or compositional fault frictional properties, or differences in fault architecture or structural evolution, perhaps associated with seamount subduction (Wang & Bilek 2014).

3 MODELLING STRATEGY

The present-day margin morphology and rock properties derived from seismic velocity profiles are used as initial conditions in

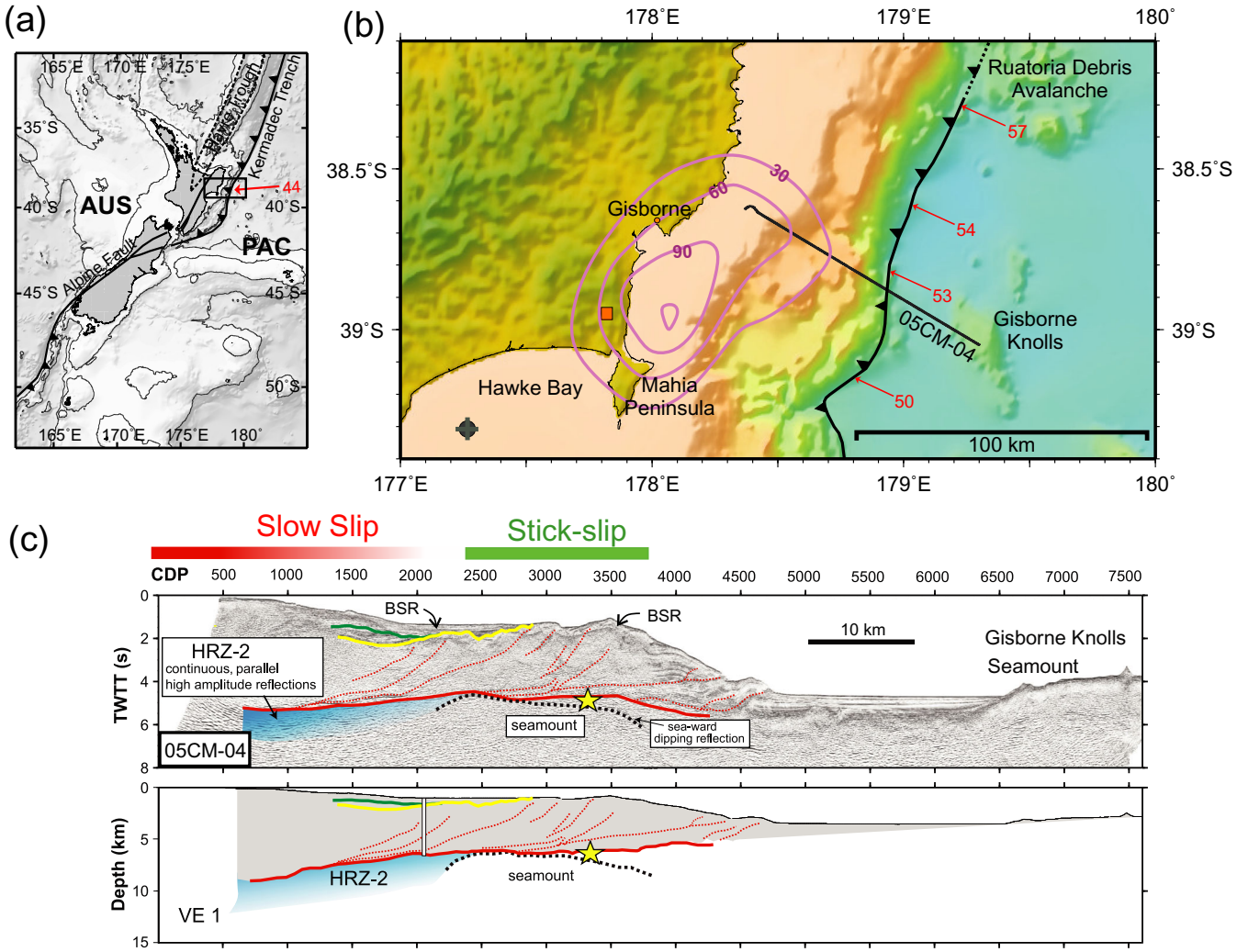

Figure 1. (a) Tectonic setting of the Hikurangi subduction margin on the East Coast of the North Island. AUS, Australian Plate; PAC, Pacific Plate. Red arrow on inset indicates Pacific/Australia relative velocity vector in mm yr^{-1} (Beavan *et al.* 2002). (b) Closeup (box in a) showing location of seismic profile 05CM-04 offshore Gisborne, New Zealand. Purple contours and numbers (in mm) show inferred interface displacement during March 2010 slow slip event (Wallace & Beavan 2010). Red arrows are convergence rates and directions between eastern North Island and Pacific Plate at trench derived from GPS in mm yr^{-1} (Wallace *et al.* 2012). Orange square marks location of Morere thermal springs from which gases with an abnormally high mantle component have been measured (Reyes *et al.* 2010). Grey circle with cross is location of Hawke Bay-1 well mentioned in text. (c) (top) interpreted seismic profile 05CM-04. Red line is subduction interface, yellow line marks base of well-stratified sediments, green line is an unconformity within stratified sediments. Dashed red lines are major splay faults and dashed black line is inferred top of subducting seamount. Yellow star marks the estimated hypocentre of the March 1947 tsunamigenic earthquake (Doser & Webb 2003). BSR, bottom simulating reflector. Blue shaded zone is region of high-amplitude reflectivity (HRZ-2) discussed in Bell *et al.* (2010). Coloured bars at top show regions of slow-slip and stick-slip inferred from GPS. (bottom) Depth converted interpretation based on velocity model in Barker *et al.* (2009).

numerical models. On timescales of less than 100 kyr, the dynamics of the wedge will not change significantly, and so we can compute the dynamic steady-state behaviour of rock and fluid advection. The advantage of this approach is that many more parameters are able to be constrained than in more generic wedge/fluid models. However, this approach also presents some challenges. A fully coupled model of rock and fluid transport starting from the present-day configuration is not possible, because a steady-state solution will be non-unique. Attempts to solve for coupled steady-state fluid pressure and rock deformation develop instabilities where fluid pressures are initially out of balance with overburden pressure and locally become supra-lithostatic, causing unstable mechanical deformation. This occurs because there is two-way coupling between fluid pressure and rock deformation; the flow of rock through the wedge causes compaction and porosity changes creating excess fluid that must flow to the surface and can locally increase fluid pressure; but fluid pressure changes the effective stress of the material and alters its frictional behaviour, thus feeding back into rock deformation.

To get around this problem, we firstly model wedge mechanics assuming a constant fluid pressure ratio of 0.65, as described in Section 4. Frictional parameters of modelled sediment are chosen to give a mechanical behaviour consistent with a stable wedge morphology and locus of deformation. We use this model to compute fluid release from compaction-associated porosity changes as material flows through the wedge and fluid generation from dehydration reactions with increasing temperature. These fluid budgets are used in Section 5 to constrain a steady-state fluid-flow model through the wedge. The two models are linked in the discussion by considering

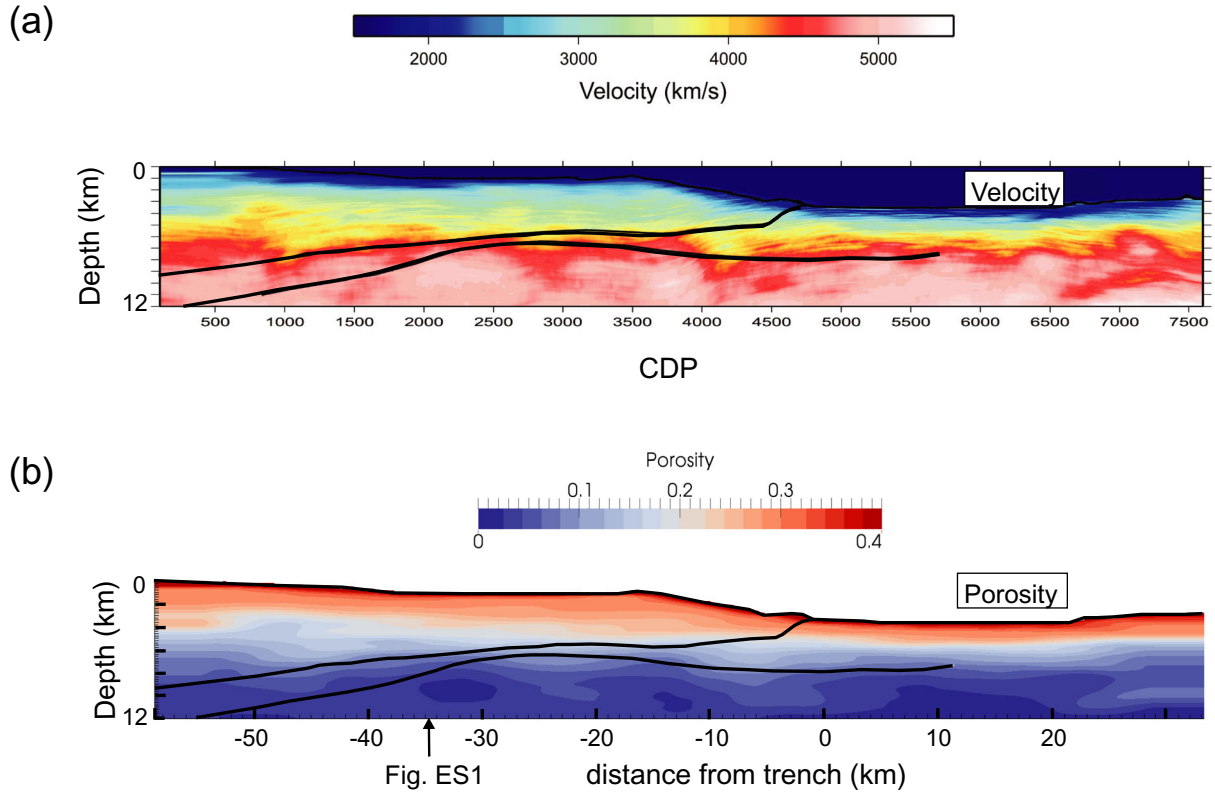

Figure 2. (a) *P*-wave velocity determined for line 05CM-04 using HDVA as discussed in the text. A horizontal smoothing window of 1500 m was applied. Black lines show picks to the décollement and basement derived from seismic interpretation. (b) Porosity derived from (a) using the method of Erickson & Jarrard (1998). The black arrow shows the location of the profiles in Electronic Supplement 1.

the effect that a non-constant fluid-pressure ratio (as in Section 5) has on mechanics in the wedge.

4 FLUID BUDGETS DERIVED FROM WEDGE DYNAMICS

We constrain our model with porosities and geometry derived from line 05CM-04, and compute thermal structure and sediment transport (*cf.* Bekins & Dreiss 1992). We use a mechanical model coupled to conductive heat-flow to model the advection of material through and beneath the wedge. As discussed in Section 3, the model is a 'snapshot' in time in that it computes velocity and deformation of sediment and rock for the present-day geometry and material properties of northern Hikurangi. We do not model seismic rupture or transient slow slip; that is, our computed material flow is averaged over one or more seismic/interseismic slip cycles. The material flow-field is used to directly estimate fluid release caused by compaction (porosity loss), and opal and clay dehydration reactions. Each of these steps is described in more detail below.

4.1 Constraints from multichannel seismic data

We base our calculations on multichannel seismic reflection data from line 4 of the 05CM survey conducted by Crown Minerals in 2005 (Barker *et al.* 2009; Fig. 1c). Three independent velocity analyses were performed (high density velocity analysis, which uses automated normal moveout; and two different iterations of prestack depth migration). These independent velocity analyses showed relatively minor differences (Electronic Supplement 1). Fig. 2(a) shows the HDVA picks, based on velocity changes and reflectivity, to the top of subducted sediment and to high-velocity basement along this line (Barker *et al.* 2009). A small amount of horizontal averaging (smoothing) was used, with a smoothing window of *ca*. 1500 m. Changes in velocity, a variation in amplitude reflectivity at depth, and magnetic anomalies have been used to infer the presence of a subducted seamount (Bell *et al.* 2010). The profile is thought to cross the flank of a somewhat oblique, linear seamount rather than intersecting it at its crest.

Porosity can be calculated from the compressional wave velocities (*Vp*) or density derived from *Vp* along this line. Density was determined using two different methods (Gardner *et al.* 1974; Brocher 2005). Four different methods of calculating porosity were tested: the first two use the normal and high compaction history equations of Erickson & Jarrard (1998) to directly relate *Vp* and porosity (e.g. Hoffman & Tobin 2004; Calahorrano *et al.* 2008; Tobin & Saffer 2009); the last two methods derive porosity indirectly from density following Brocher (2005) and Gardner *et al.* (1974), assuming a shale fraction of 0.3, a particle density of 2750 kg m^{-3}, and water density of 1000 kg m^{-3}. In Fig. 2(b), we show the porosity derived from the normal compaction relationship of Erickson & Jarrard (1998). Other methods yield similar results (Electronic Supplement 1); the Brocher (2005) density-porosity had the highest porosities at depth (Fig. ES1c). The 'normal compaction' Erickson & Jarrard (1998) porosity model is used in this paper, but we also compared it to predicted compaction-related fluid release using the 'high porosity' end-member and found that results did not differ significantly. A common feature of all porosity transformations is that they show little change in porosity across the deformation front (i.e. near the wedge toe) so that fairly high porosities are maintained within the wedge, as was also noted by Bassett *et al.* (2014).

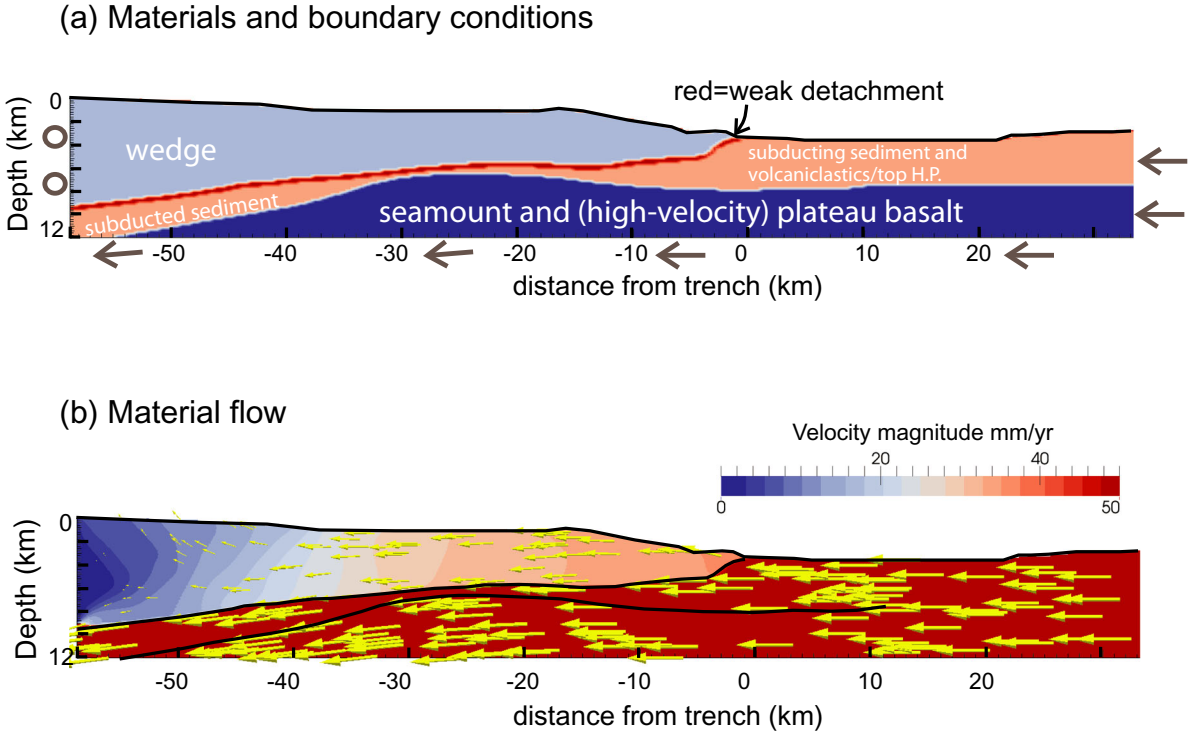

Figure 3. Thermomechanical numerical model setup for Section 4. (a) Materials and boundary conditions (described in text). See Table 1 for material properties as labelled (seamount and plateau basalt have same properties). (b) Modelled flow of material through the wedge; colour contours and vectors show velocity field.

4.2 Thermomechanical modelling

The geometry along seismic line 05CM-04 is used to construct a 2-D mechanical model for a 120-km-long transect perpendicular to the trench using finite-element code SULEC (Ellis *et al.* 2011; Buiter & Ellis 2012). We model pressure-sensitive frictional plastic flow based on a Coulomb yield criterion, and allow large strain to develop by tracking strain and other quantities on tracer particles (Fig. 3a). In the thermo-mechanical models we prescribed material layers simplified from Fig. 2(a). Note that the incoming 'sediment' layer includes Cenozoic–Mesozoic sediment, volcaniclastic sediment with interbedded basalt and the older sequence HKB (Cretaceous volcaniclastics and/or limestone/chert) at the top of the basaltic Hikurangi Plateau as described in Davy *et al.* (2008). Boundary conditions representing the subduction velocity component normal to the margin (5 cm yr^{-1}) are applied at the right-hand boundary, along the base, and along the lowermost 3 km of the left-hand boundary. Above this, the left-hand boundary horizontal velocity is prescribed to be zero, while vertical velocity is free, as indicated by circles. The outlet velocity is gradually adjusted along the base so that at the left-hand side of the model it is at the same angle as the weak detachment, while at the right-hand side it is horizontal. Outward material flux is 80 per cent of incoming flux, so that the top 2 km of material accretes to the wedge. The 2 km thickness is derived from the depth to the subhorizontal décollement picked on line 05CM-04, just before it steps up at the toe of the wedge, and where the sediment/HKB sequence has been thickened as it approaches the trench (Fig. 2a). Material frictional strength is a function of effective pressure and sediment type (Table 1). A layer with negligible viscosity is used to represent the weight and fluid pressure of overlying seawater. A constant fluid pressure ratio higher than hydrostatic ($\lambda = 0.65$; Bassett *et al.* (2014)) is assumed throughout the wedge, where:

$$\lambda = \frac{(p_f - \rho_w g D)}{(\sigma_z - \rho_w g D)} \quad (1)$$

is the modified Hubbert–Rubey fluid pressure ratio corrected for water depth, D. p_f is fluid pressure, σ_z is the vertical normal stress,

Table 1. Frictional and thermal properties used in the initial 2-D thermomechanical model.

	'Dry' angle of internal friction, ϕ^a	Effective angle of internal friction ($\lambda = 0.65$)^b	Cohesion (MPa)	Density (kg m^{-3}) and thermal conductivity (W m^{-1} K^{-1})
Wedge	40° (0.83)	16°	0.01	From seismic reflection analysis as described in text
Subduction interface	8.5° (0.15)	3°	0	
Subducted sediment	40° (0.83)	16°	0.01	
Oceanic crust (seamount and slab)	40° (0.83)	16°	10	

[a]Values in brackets are friction coefficient.
[b]Effective friction angle computed as atan[$(1 - \lambda)$tan(ϕ)], assuming a constant pore fluid pressure ratio λ of 0.65 (Bassett *et al.* 2014) in Section 3. See Electronic Supplement 2 for a sensitivity study of wedge mechanics for different frictional strengths of the subduction interface.

g is gravity and ρ_w is fluid density (Hubbert & Rubey 1959; Davis *et al.* 1983; Dahlen 1984).

The subduction interface is prescribed as a continuous, low-strength layer or décollement with a dry frictional coefficient of 0.15 (Table 1). The low value of décollement friction produces thickening at the toe of the accretionary wedge, consistent with preliminary reconstructions of line 05CM-04 through the last million years, which show that most of the thickening and shortening of the wedge has been focused on the outermost few imbricate thrust slices as described above (Barker *et al.* 2009) and as is common at many subduction margins (e.g. Morgan & Karig 1995; Moore *et al.* 2011). Models of wedge deformation and material flow for higher values of décollement friction produce shortening near the backstop of the model, which is inconsistent with observations (Electronic Supplement 2). In practice, as noted by Bassett *et al.* (2014) the wedge is unlikely to be at a compressive critical taper, owing to the passing of the seamount through the system over the past *ca*. 0.8 Ma; mechanical models over longer timescales show how the region landward of a subducting seamount can be almost flat, while the zone seaward of it is significantly oversteepened (Electronic Supplement 4). The simple mechanical setup used here is our best approximation for the type of deformation above a subducting seamount seen in Fig. ES4.

In order to compute release of fluid from opal and clay dehydration in the subducting and accreting sediment, the numerical code also solves the steady-state heat-flow equation, taking material advection into account. No radiogenic heating or shear heating is applied and heat advection by fluids is neglected. The assumption of negligible shear heating is consistent with constraints requiring low strength along the detachment (as noted above). We assume a basal heat-flow of 45 mW m^{-2} (Townend 1997b; Henrys *et al.* 2003). Thermal conductivity is computed from the porosity field of Fig. 2(b) using the relationship:

$$k = k_s^n k_r^{(1-n)}, \tag{2}$$

where n is porosity, and k is the geometrically averaged thermal conductivity derived from thermal conductivity of seawater (k_s, 0.67 Wm^{-1} K^{-1}) and of rock grains (k_r, 2.8 Wm^{-1} K^{-1}; Pecher *et al.* 2010). The seafloor is prescribed a constant temperature (derived for an average depth of 1 km for most of the wedge) of 4°C (Ridgway 1969). Because we model the shallow wedge and not the entire subduction system, these calculations only encompass the simplest approximation of the Hikurangi margin thermal structure; however, we are able to roughly match heatflow estimates based on gas hydrate BSRs, which show a decrease from *ca*. 45 mW m^{-2} at the trench to *ca*. 35 mW m^{-2} 100 km landward caused by the downward advection of heat and thickening of the margin (Field *et al.* 1997; Townend 1997b; Henrys *et al.* 2003; Fagereng & Ellis 2009). We predict temperatures of *ca*. 150 °C at 12 km depth and a thermal gradient there of about 12–15 °C km^{-1}, consistent with previous thermal models (e.g. Fagereng & Ellis 2009) and an estimated interface temperature of *ca*. 170–200 °C at 15 km depth for the Hawke Bay-1 well further south (Henrys *et al.* 2006).

The resulting material flow is shown in Fig. 3(b). For the present-day geometry from line 05CM-04 and a weak décollement, we predict a mostly stable wedge with thickening and accretion concentrated at the toe, consistent with structural observations and similar to the evolutionary models with seamounts shown in Fig. ES4. As noted above, higher friction values for the décollement (e.g. Electronic Supplement; Rowe *et al.* 2012) are inconsistent with deformation focused at the toe of the wedge. The model results based on Table 1 parameter values are used in the next section to compute fluid release as material subducts beneath and is incorporated within the wedge.

4.3 Compaction fluid sources

Accreting and subducting sediment loses water by compaction, because net reduction in porosity leads to expulsion of fluids. Sediment also releases fluid from metamorphic dehydration reactions as temperature increases. Previous estimates of fluid release for the Hikurangi margin are based on bulk calculations that use margin-averaged estimates for temperature gradients, rates of accretion and subduction (Townend 1997a; Pecher *et al.* 2010). Here, we use the results from the mechanical model to calculate fluid production from porosity reduction and increasing temperature and pressure at each point along profile 05CM-04. We combine the spatial gradient in the porosity field derived from seismic reflections (Fig. 2b) with the material flow-field from the mechanical model (Fig. 3b), assuming that porosity is in steady-state; that is, the profile has a fixed porosity field through which sediments move so that the distribution shown in Fig. 2(b) is constant in space, so that the local time derivative of porosity is zero (e.g. Bethke 1986; Bekins & Dreiss 1992; Wang 1994). In reality, this is unlikely to be true, particularly since the subducting seamount is advecting along with the lower plate, transiently affecting the compaction and subduction of sediment around it. For this reason, calculated rates are probably best regarded as modern (rather than long-term) estimates of compaction-related fluid release. We calculate fluid release from porosity reduction as:

$$\frac{\mathrm{d}V}{\mathrm{d}t} = \frac{1}{(1-n)}\left(u\frac{\mathrm{d}n}{\mathrm{d}x} + v\frac{\mathrm{d}n}{\mathrm{d}y}\right), \tag{3}$$

(Bekins & Dreiss 1992) where n is porosity at each point derived from seismic reflectivity, u and v are horizontal and vertical velocities derived from the mechanical model, and $\frac{\mathrm{d}V}{\mathrm{d}t}$ is fluid release (m^3 fluid m^{-3} rock per second)for a unit metre along-strike. Since the vertical sediment velocity v is small compared to the horizontal velocity u, the fluid release from porosity reduction depends mainly on the horizontal porosity gradient dn/dx. Before deriving fluid release from (3), we apply further horizontal smoothing (with a sample window of 7.5 km) to the porosity field to remove some of the small-scale fluctuations apparent in Fig. 2(b). This reduces the peak amplitude of fluid release slightly, but does not change the location of maximum volume change. Compaction-related fluid release from the high-velocity subducting oceanic crust is not considered in the models.

Fig. 4(a) shows the fluid source term calculated for the 05CM-04 line assuming the material flow-field from Fig. 3(b). Owing to the smoothly varying material flow field transporting material from right to left, most of the variation in volumetric fluid release in eq. (3) arises from the spatial gradients in porosity (Fig. ES3). The most conspicuous features are zones of high fluid release just seaward of the seamount in the subducted sediment *ca*. 10 km landward of the trench; and above the seamount in the wedge. Some regions show fluid sinks (negative fluid release): at the toe of the wedge, where rapid uplift of material occurs; and within the incoming sediment column and near the backstop of the model. We interpret them as artefacts that occur partly because porosity is not decreasing monotonically landward due to small-scale lateral variations (as seen in Fig. 2b). These are unlikely to reflect actual expansion of the sediment matrix (i.e. porosity increase) as it is transported arcward in the forearc, and instead probably represent spatial variability in porosity that limits the reliability of fluid source calculations at

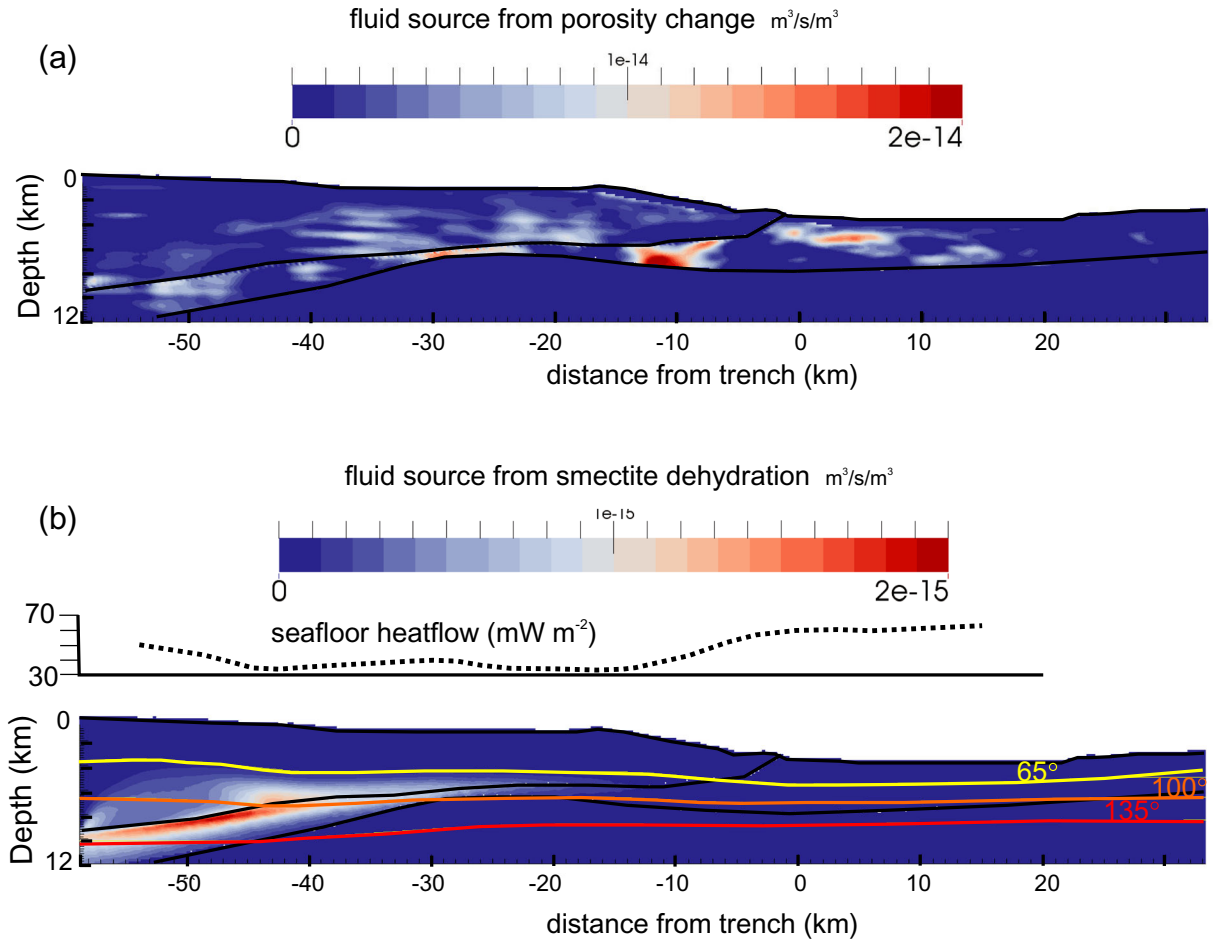

Figure 4. Fluid production rates for Section 4 predicted from the numerical model. Black lines show picks to detachment and basement. (a) Fluid sources from the change in porosity as material moves through the wedge, assuming a steady-state porosity distribution. Note that top zone of wedge with porosity >0.3 is excluded from fluid release calculation to avoid interpolation errors from water to sediment. (b) Fluid sources from dehydration of smectite to illite. Model has been run until temperature and smectite distribution attain advective steady-state. Colour contours show isotherms and dashed line above model shows predicted heat-flow near seafloor, which decreases from 60 m Wm^{-2} at the trench to 35 mW m^{-2} further landward.

high spatial resolution; previous applications of this approach (e.g. Bekins & Dreiss 1992) have typically assumed a smoothly varying porosity reduction with burial, rather than defining a detailed porosity distribution from observations. To some extent, lateral variations in apparent porosity may also reflect uncertainty in estimates of porosity from *P*-wave velocity. The lack of significant velocity (and thus computed porosity) change near the toe may represent undrained conditions during initial loading (i.e. compaction disequilibrium), or some other effect of deformation and/or elevated fluid pressure; we discuss this further in Section 6.

4.4 Dehydration reactions and fluid budgets

Following Saffer *et al.* (2008) we use the kinetic reaction model of Pytte & Reynolds (1988) to compute the transformation of smectite in the wedge and subducting sediments, using the steady-state temperature field, and the material flow-field of the mechanical model (Fig. 3b). The material derivative (the change in smectite content of a tracked material point with time, assuming constant potassium content) is given by:

$$\frac{\mathrm{D}S}{\mathrm{D}t} = -C_1 S^5 \exp\left(\frac{-C_2}{T}\right), \tag{4}$$

where S is the mole fraction of smectite in the mixed-layer illite-smectite (I/S) clay component of the sediment, T is temperature in Kelvin and C_1 and C_2 are constants (3.9×10^9 s^{-1} and $-19\,089$ K, respectively; derived from Pytte & Reynolds 1988, and incorporating the activity of potassium into constant C_1 assuming equilibrium between albite and K-feldspar). At steady-state, the local (Eulerian) time derivative is zero so that the material derivative is balanced by the advective rate of smectite change:

$$C_1 S^5 \exp\left(\frac{-C_2}{T}\right) = \left(u\frac{\mathrm{d}S}{\mathrm{d}x} + v\frac{\mathrm{d}S}{\mathrm{d}y}\right), \tag{5}$$

where u, v are the 2-D velocities. We solve this equation iteratively for molar fraction S and the associated steady-state fluid release. We assume an initial smectite weight fraction F at shallow depths of 20 per cent in incoming sediments (Pecher *et al.* 2010). We take an initial mole fraction of S in mixed I/S of 1.0, which decreases with depth (temperature). That is, we assume that the smectite-clay molar fraction in incoming sediment and slab has equilibrated with the local temperature field for 1 Myr prior to entering the margin so that the smectite-illite reaction is already underway (as a function of temperature) when material enters the trench, yielding a reduction in the smectite mole fraction with depth in the incoming section.

Fig. 4(b) shows colour contours of associated fluid release in units of $m^3\ s^{-1}\ m^{-3}$ calculated from eq. (6) at thermal steady state including rock advection, where we take $W = 0.35$ volumetric fraction of water bound in the hydrated smectite that is available to be released upon transition to illite. We assume a hydration state with two water interlayers and a 15 Å d-spacing, as is common in marine sediments (Colten-Bradley 1987; Fitts & Brown 1999):

$$\frac{\mathrm{d}V}{\mathrm{d}t} = WFC_1S^5 \exp\left(\frac{-C_2}{T}\right)(1-n). \tag{6}$$

The effects of rock advection in the downgoing slab and subducting sediment depresses both temperature and the transition at which smectite to illite transition occurs (owing to the rate-dependence of smectite transformation and material advection). Results suggest that the transition from smectite to illite is gradual; it begins about 40 km landward of the trench and continues landward of the 05CM-04 seismic section, with about 75 per cent of the incoming smectite converted to illite over a temperature range of *ca*. 80–135 °C.

We used a similar approach to test whether fluid release from the metamorphic transition of opal to quartz is significant, based on the reaction kinetics derived from laboratory experiments in Ernst & Calvert (1969). An initial opal content of 10 wt%, decreasing with temperature (assuming equilibrium at that temperature for 1 Myr) was prescribed within the incoming sediment layer. Opal diagenesis runs to completion at temperatures greater than ∼100 °C, so the fluid release from this reaction occurs in the shallow part of the wedge, and is an order of magnitude smaller than the fluid production from smectite reactions. It is not shown in Fig. 4.

Dehydration reactions may also occur in the subducting basaltic crust of the Hikurangi Plateau. The composition of the plateau crust is comparable to the Ontong-Java Plateau and representative of N-MORB tholeiitic basalt (Hoernle *et al.* 2010), so that it does not differ significantly from normal mid-ocean ridge basalt. There is, however, a question of how the hydration state of Hikurangi plateau compares to normal, thinner, oceanic crust, and future dredging and drilling programmes may address this. We assume that hydrous phases in the Hikurangi Plateau are saponite and zeolites formed by sea floor hydration and alteration. Zeolites will dehydrate to form greenschist facies minerals at 300 °C or more (e.g. Kerrick & Connolly 2001; Hacker *et al.* 2003; Fagereng & Diener 2011), retaining their crystal-bound water beyond the modelling domain considered here. Similarly, saponite carries a significant crystal-bound water content into the subduction zone (Kameda *et al.* 2011), but predominantly dehydrates at temperatures in excess of 200 °C (Hillier 1993), and then to create chlorite which itself is more hydrous than illite-muscovite. Dehydration of the oceanic crust may therefore contribute to the fluid budget in the Hikurangi margin at depths greater than 15–20 km, and maybe at shallower levels if the released fluids flow along the decollement. For the depth range considered in this paper, however, we have chosen to ignore the contribution from basaltic crust of the Hikurangi Plateau.

4.5 Integrated fluid production and comparison with previous estimates for the Hikurangi Margin

The estimates in compaction-derived fluid release from Section 4.3 predict small-scale fluctuations that result from short wavelength variations in the porosity field derived from the seismic reflection analysis. Some of these fluctuations are likely to be caused by changes in the incoming sediment layering, properties, and thickness through time, and are probably not steady-state features, or are artefacts associated with uncertainty in estimating porosity from *Vp*. In addition, the subduction of seamounts in this region is a transient phenomenon on the scale of hundreds of thousands of years, so that porosity loss may be more localised and transient than for subduction margins with smoother interface topography. Nevertheless, previous estimates of fluid release from compaction across the Hikurangi system averaged along-strike have assumed initial porosities as high as 0.55 in incoming sediment reducing to less than 0.1 after accretion (Pecher *et al.* 2010). Such large changes in porosity are not evident along the northern Hikurangi margin. In particular, the porosity field of Fig. 2(b) shows no major change in porosity across the toe of the wedge. This seems inconsistent with interpretations that deformation is currently concentrated in the outer-most few thrust slices along the profile (e.g. Pedley *et al.* 2010). Unless deformation is completely concentrated along faults, there ought to be a component of compactive strain associated with this deformation. One possible explanation is that *Vp* stays low in the toe of the wedge because of intense damage/fracturing there, in which case the matrix porosity may well be decreasing (causing wedge drainage) but the predicted increase in *Vp* is offset by damage sampled at seismic wavelengths (e.g. Gettemy *et al.* 2004). This region may also experience periodic compressive stress release in the wake of subducting seamounts (Dominguez *et al.* 2000). Alternatively, pore space may remain open due to low effective stresses because of high pore fluid pressures there (Bassett *et al.* 2014).

We consider integrated rates of fluid production along profile 05CM-04 by combining the results from Sections 4.3 and 4.4 for different regions of the subduction system (Table 2; Fig. 5). For comparison with previous studies, we divide the profile into the following subdomains: the wedge (region I); the subducting sediment between trench and seamount (region II, $x = -20$ to 0 km); the subducting sediment above the seamount (region III, $x = -40$ to -20 km); and subducting sediment landward of the seamount (region IV, $x = -60$ to -40 km). The relative thicknesses of sediment destined to be accreted or subducted at the toe, along with the amount of incoming water bound in clay and in pore spaces, are computed from averages over $x = -2$ to 10 km, and assuming that all material above the white dashed line in Fig. 5(a) is accreted, consistent with the material flow computed in Section 4. Regions with porosity increasing in the direction of flow have fluid sources set to zero. In Table 2 we use the same terminology as Pecher *et al.* (2010), where the symbol h refers to thickness of incoming layers (subscripts *accr* = accreted, *sub* = subducted); V refers to volumes of fluid entering and released from the system (subscripts *accr*, *hydac* = accreted and bound to hydrous minerals, *sub*, *hydsub* = subducted and bound to hydrous minerals; *comp* = released from compaction, *hydaccrel* = released from dehydration reactions, and *compsub, hydsubrel* are released from subducting sediment). Note however, that the comparison in Table 2 is between our estimates for a particular profile (the northern margin) and margin-wide averages in Townend (1997a) and Pecher *et al.* (2010).

Table 2 shows several surprising features in our analysis compared to previous estimates of fluid productivity for the Hikurangi Margin. We find roughly half as much fluid production in the wedge from compaction (porosity reduction; V_{comp}). This is because the changes in porosity from incoming sediment column to wedge estimated via seismic reflectivity are less than those averaged for the entire Hikurangi margin by Pecher *et al.* (2010) and Townend (1997a). In addition, the mechanical model and reconstructions of the northern margin show that most of the accretion is occurring at the toe of the wedge; inspection of Fig. 2(b) shows little change in average porosity across this region. Our study suggests that water release from subducting sediment is actually higher than that

Table 2. Prescribed parameter values and resulting fluid production in this study for line 05CM-04 compared with previous estimates for the Hikurangi Margin (note that previous estimates are averages along-strike, whereas our values are for northern Hikurangi).

	This study (line 05CM-04)	Pecher *et al.* (2010)	Townend (1997a)
Thickness of accreting sediment, h_{accr} (m)	912	2200	1500
Thickness of subducting sediment and volcaniclastic layers, h_{sub} (m)	2200	900	–
Initial porosity of incoming accreting (and subducting) layers	0.27 (0.12)	0.55 (–)	0.4 (–)
Final porosity of compacted sediments in wedge	*ca*. 0.3–0.1	0.1	0.1
Final porosity of subducting sediment	<0.05	0.35	–
Clay weight fraction in incoming sediment (F)	0.2	0.2	0.2
Water fraction in smectite (W)	0.35	0.35	0.35
Subduction velocity normal to trench m yr^{-1}	0.05	0.035	0.04
Integrated fluid (pore, bound in clay, total) entering trench from accreting sediment[a] m^3 yr^{-1} m^{-1}	$V_{accr} = 12.2$ $V_{hydac} = 2.2$ Total = 14.4	$V_{accr} = 42$ $V_{hydac} = 2.4$ Total = 44.4	$V_{accr} = 24$ $V_{hydac} = 3$ Total = 27
Integrated fluid (pore, bound in clay, total) entering trench from subducting sediment[a] m^3 yr^{-1} m^{-1}	$V_{sub} = 13.4$ $V_{hydsub} = 2.5$ Total = 15.9	$V_{sub} = 11$ $V_{hydsub} = 1.4$ Total = 12.4	–
	Total ~ 30 m^3 yr^{-1} m^{-1}	Total ~ 57 m^3 yr^{-1} m^{-1}	Total ~ 27 m^3 yr^{-1} m^{-1}
Integrated volumetric fluid release in wedge (region 1) from porosity change[b] m^3 yr^{-1} m^{-1}	$V_{comp} = 12.6$	$V_{comp} = 39$	$V_{comp} = 20$
Integrated volumetric fluid release in wedge (region 1) from smectite to illite transformation (and opal) m^3 yr^{-1} m^{-1}	$V_{hydaccrel} = 1.2$ (0.3)	–	–
Integrated volumetric fluid release in subducting sediment (regions 2, 3 and 4) from porosity change m^3 yr^{-1} m^{-1}	$V_{compsub} = 13.9$ Region II (near trench): 6.6 Region III (above seamount): 3.6 Region IV (landward of seamount): 3.7	–	–
Integrated volumetric fluid release in regions III and IV from smectite to illite transition m^3 yr^{-1} m^{-1}	$V_{hydsubrel} = 1.8$ Region III (above seamount): 0.4 Region IV (landward of seamount): 1.4 Total ~ 30 m^3 yr^{-1} m^{-1}	–	–
% incoming pore-bound fluid released in wedge and subducted sediment $(V_{comp} + V_{compsub})/(V_{accr} + V_{sub})$	100 per cent	–	–
% incoming clay-bound fluid in subducted sediment released at depth $(V_{hydsubrel})/(V_{hydsub})$	73 per cent	–	–

[a]Derived from spatially averaged porosity in material above/below décollement entering subduction system, and assuming 35 per cent water tied up in smectite, that clay makes up 20 per cent of incoming non-porous sediment layer on average, and using calculated initial smectite/illite ratio as described in text for initial equilibration time of 1 Myr.
[b]Note that top zone of wedge with porosity >0.3 is excluded from fluid release calculation to avoid interpolation errors from water to sediment.

within the wedge, most likely because the total thickness (and thus fluid inventory) of the subducting section is substantially larger than previous assumed (Table 2). The dewatering of the subducted sediment occurs mostly beneath the steep outer wedge slope and above the subducting seamount, where the section becomes substantially thinner with increasing burial depth (Fig. 5b, regions II and III).

The calculated fluid entering the subduction system bound to smectite (Table 2; V_{hydac}, V_{hydsub}) is mostly in the sediment destined to be subducted beneath the wedge, because this sediment is thicker than overlying (to be accreted) layers, and the volumetric fraction of solid rock containing clay-bound water in the sediment increases with decreasing porosity. The total modelled fluid release owing to clay dehydration in regions III and IV is less than the total clay-bound water entering the system (75 per cent), indicating that some of this is lost further landward than our modelled region. The use of the thermo-mechanical model allows us to predict that the dehydration reaction peaks *ca*. 40–50 km landward of the trench at depths of around 10 km, and that it is concentrated near the top of the subducted sediment above and landward of the subducting seamount, between temperatures of 80 and 150 °C (Fig. 4b). These temperatures are comparable to the 60–150 °C range estimated for smectite dehydration elsewhere (e.g. Saffer *et al.* 2008; Saffer & Tobin 2011), although the onset of dehydration in the model occurs at slightly higher temperatures, since faster convergence rates move the dehydration peak to greater depths owing to advection of clay downward within the underthrust sediment. Dehydration of smectite produces fluid at a rate per volume an order of magnitude less than peak production from porosity changes (Figs 5c versus b), but the fluid release is sustained over a larger region at depth (e.g. Bekins *et al.* 1995). As a result, the integrated effect of dehydration reactions in region IV, while only half of the fluid released there from porosity changes, is still a significant source of fluid (Table 2; Fig. 6a). Since the effect of fluid sources on overpressure development is also influence by flow path distance and permeability

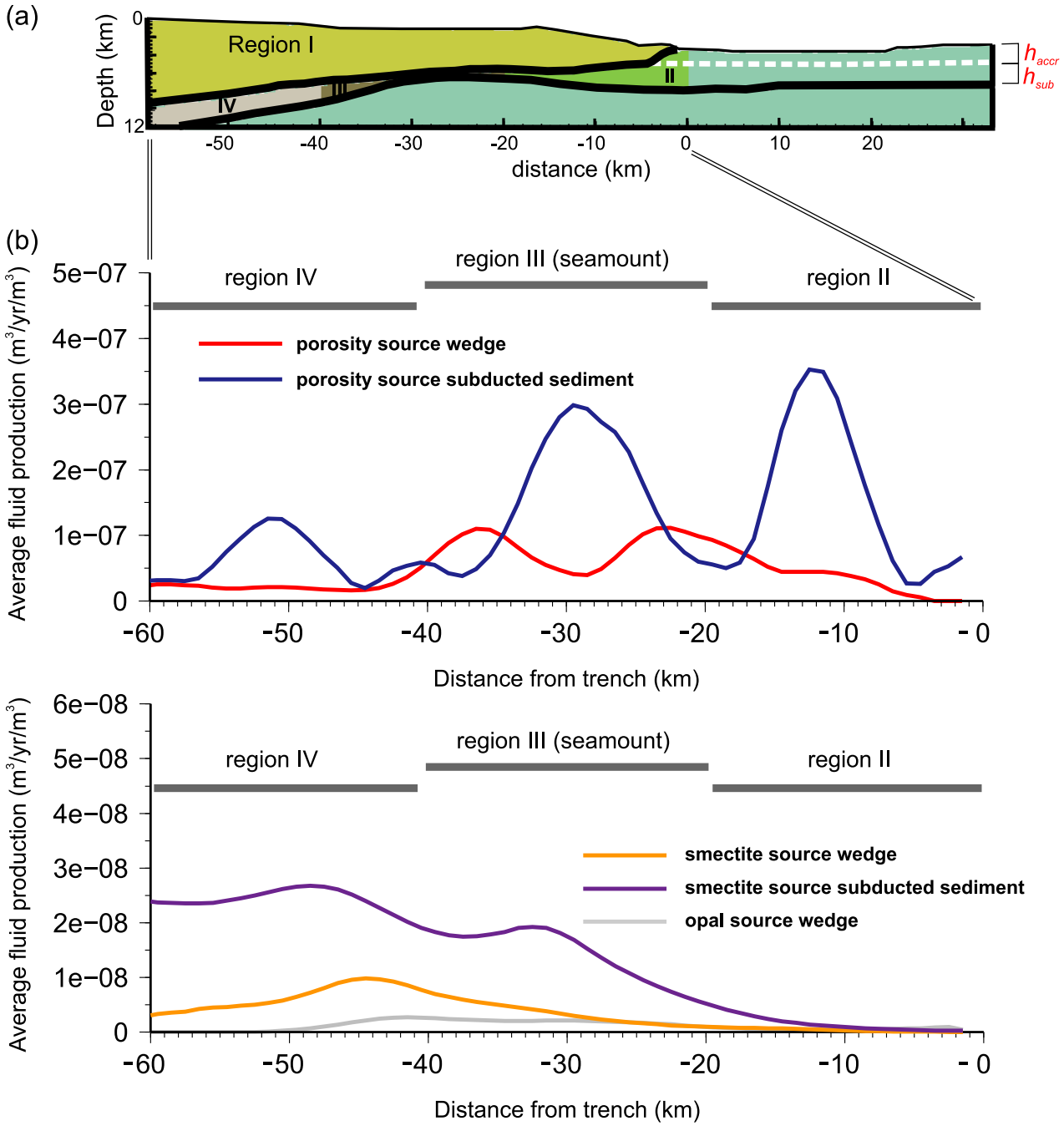

Figure 5. (a) Colour-coded regions referred to for integrating fluid production in Figs 5 and 6 and Table 2, and definitions of incoming thicknesses (h_{accr}, h_{sub}) as used in Table 2. (b) Average volumetric fluid production in the wedge (Region I) and subducted sediment (Regions II, III and IV) from porosity changes. (b) Average volumetric fluid production from dehydration reactions.

along that path (Neuzil 1995), there is also a commensurately larger impact of fluid sources from greater depth, as is seen later in the fluid-flow modelling (Section 5).

Note that the fluid production estimated from clay dehydration depends critically on the assumed clay fraction and smectite distribution within incoming sediment. The results shown here assume that clay makes up 20 wt% of incoming sediment on average, and compute an initial smectite-illite fraction that assumes reactions have occurred for at least 1 Myr in incoming sediment. If more smectite were initially present within incoming sediment at 2–4 km depth, and thus was subducted to depth beneath the wedge, the fluid release from dehydration reactions would form a higher proportion of total fluid released. Deep boreholes and better estimates of incoming sediment composition are critically needed to more accurately constrain the fluid production from clay dehydration reactions at depth along 05CM-04.

Moore *et al.* (2011) compute fluid production rates from porosity loss for the Nankai margin based on structural restorations in the accretionary prism and underthrust sediments, and compare cumulative dewatering rates with distance from the trench for the Aleutian, Costa Rican, Nankai and Barbados subduction zones. For Nankai, they find that most dewatering occurs in the outermost 2–6 km of

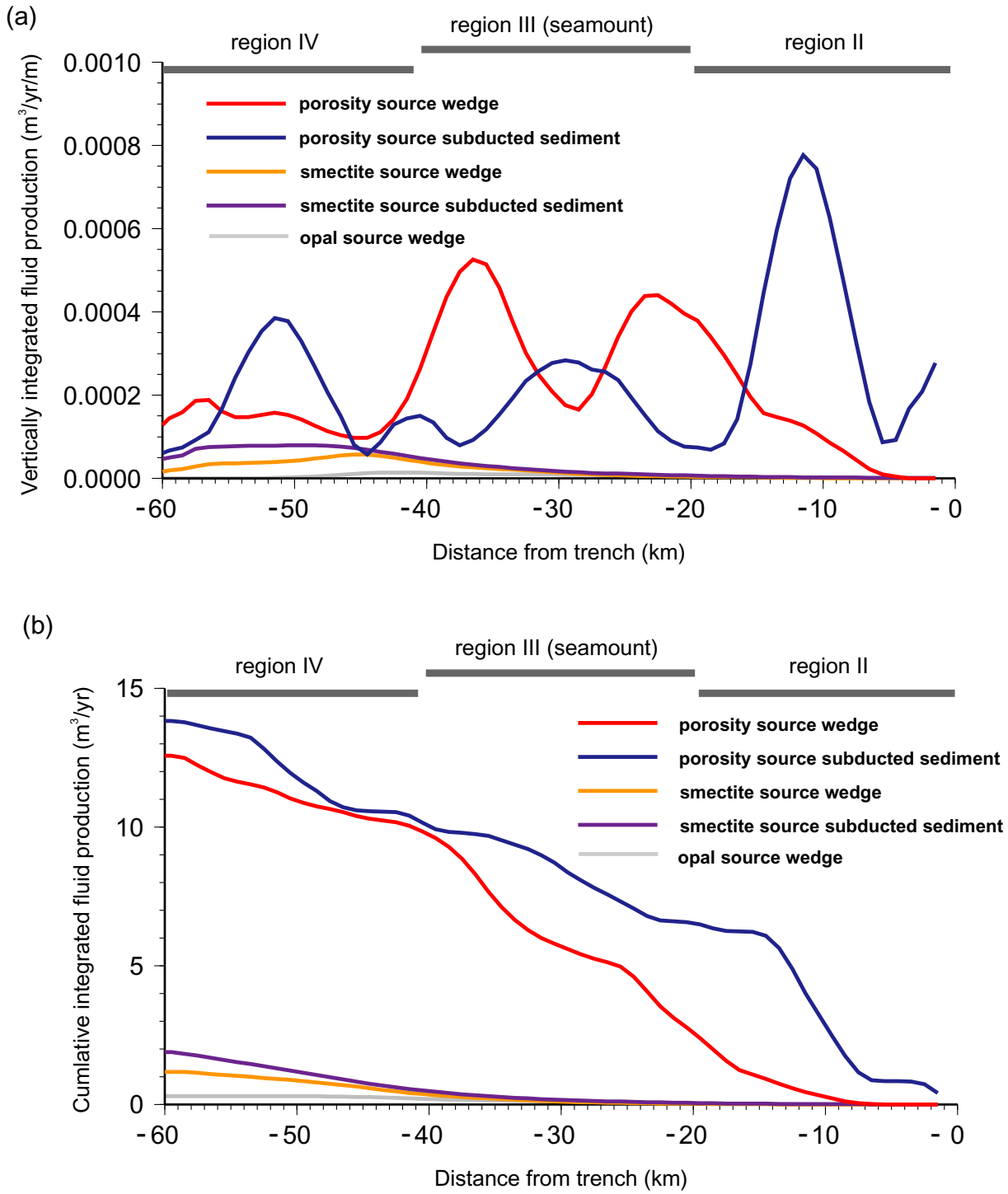

Figure 6. (a) Vertically integrated fluid production (i.e. total fluid production in vertical columns) for the wedge and subducted sediment from porosity changes and dehydration reactions. (b) Cumulative (integrated) fluid production for each region and source with distance from the trench.

the accretionary wedge (a cumulative total of *ca*. 11 m^3 yr^{-1} m^{-1}); average porosities for the Nankai wedge change by over 15 per cent (from 50 per cent to 32 per cent) over the same region. In comparison, for 05CM-04 in Hikurangi we compute a cumulative wedge dewatering rate over the total wedge (0–60 km landward of the trench) of *ca*. 13 m^3 yr^{-1} m^{-12} (Table 2 V_{comp}; Fig. 6b), but no dewatering in the first 8 km away from the trench. The porosity derived from seismic velocities (Fig. 2) does not decrease at all in the first 5 km, and vertically averaged wedge porosities only gradually decrease thereafter, from an average of about 35 per cent at the toe of the wedge to 20 per cent 50 km landward.

Within the underthrust sediments, Tobin & Saffer (2009) compute a cumulative dewatering rate from compaction of *ca*. 1 m^3 yr^{-1} m^{-1} for the Muroto transect of the Nankai subduction zone, occurring mostly within 4 km landward of the trench; Zhao *et al.* (1998) report similar estimates for Barbados. Cumulative fluid release from

subducted sediment computed for the northern Hikurangi profile is higher ($V_{compsub}$~14 m^3 yr^{-1} m^{-1}, Table 2; Fig. 6b), primarily owing to the much greater thickness (on average) of subducted sediment at northern Hikurangi in region IV compared to these localities (at Nankai the underthrust section is less than 350m thick). We predict that compaction-related water loss from the subducted sediment peaks *ca*. 12 km landward of the trench, about mid-way beneath the most steeply-tapered part of the outer wedge. Our computed values are similar to the underthrust region of the Costa Rican subduction margin which has cumulative dewatering rates reaching *ca*. 10 m^3 yr^{-1} m^{-1} (Saffer 2003). These high Costa Rican rates are attributed to a high convergence rate (almost 9 cm yr^{-1}) and a highly porous incoming sediment section (Moore *et al.* 2011). Lauer & Saffer (2012) estimate *ca*. 22 m^3 yr^{-1} m^{-12} total water entering the Costa Rican subduction zone, which is comparable to the estimate in Table 2 for northern Hikurangi.

The peak in smectite-illite dehydration within the subducted sediment occurs within the 'normal' temperature range of this reaction inferred from other margins as noted above (e.g. Saffer *et al.* 2008; Saffer & Tobin 2011). The predicted location of this peak (40–50 km landward of the trench, at depths of around 10 km) depends mostly on the calculated thermal structure of the margin, which is poorly constrained by data at present, as discussed in Section 4.2. Hotter margins such as Nankai that have a greater increase in temperature with depth predict dehydration at shallower depths and closer to the trench (Saffer & Tobin 2011; Spinelli & Harris 2011). The cool geothermal gradient along the Hikurangi subduction interface, and the present-day location of the subducted seamount in section 05CM-04, are such that clay dehydration occurs in subducted sediment directly above and landward of the seamount.

5 FLUID-FLOW MODELS

To investigate the magnitude and distribution of pore pressure in the forearc, and to gain quantitative insight into the factors that control pore pressure, we constructed fluid-flow models driven by the fluid source terms from Section 4.

Fluid pressure magnitudes depend on the competition between rates of fluid production and fluid flow (Neuzil 1995; Saffer & Tobin 2011). Values for permeability of sediment in the wedge and subducting sediments must be assumed in order to determine whether the fluid sources derived above can generate excess fluid pressure in the wedge and subducted sediment. Defining average permeability values is difficult, because large-scale structures and faults can act as fluid pathways, so that bulk permeabilities may be much higher than laboratory-derived measurements (Saffer & Tobin 2011; Lauer & Saffer 2012). Ideally, fluid flow rates should be constrained by comprehensive isotopic data and other fluid chemistry yielding independent estimates of fluid sources, mixing and residence times (e.g. Kastner *et al.* 1991; You *et al.* 1995, 1996; Sample 1996; Hensen *et al.* 2004; Saffer & Kopf 2006). Without such data, we perform sensitivity studies using fluid production rates from Section 3, and two end-member fluid flow models, to provide insight into the magnitude and distribution of fluid pressures at depth. The main variable that we explore is the effect of décollement permeability and its variation with distance from the trench.

As in Section 4, we derive subduction interface geometry and wedge morphology from depth-converted seismic interpretations of line 05CM-04, and we use the same two-dimensional model domain as in Fig. 3. We solve the equations of transient fluid until a steady-state pore pressure distribution is achieved, using the previously computed volumetric fluid production rates (Fig. 4), and no-flow conditions at the base and sides of the model. The numerical code assumes Darcy fluid flow driven by excess pressure gradients. Fluid source terms are input from Section 4. Either constant or porosity-related permeabilities are imposed, but these are modified where lithostatic fluid pressures are transiently attained, as discussed in more detail below. The models are considered to have converged to a steady-state solution when fluid pressure changes between successive steps are negligible (threshold 1 MPa typically after about 50 kyr, though most of this time is needed to evolve permeabilities in the models as discussed below). Note that we constrain the fluid production rates to be positive, so that, as for Section 4, the regions with negative fluid sources arising from artefacts of the assumed steady-state material advection through the porosity field are not included.

For both sets of simulations, we assume that the starting model permeability, k, of sediment in both the underthrust section and overriding wedge is a function of porosity, n, as derived from laboratory measurements of sediment core samples from ODP sites at other margins (e.g. Saffer & Bekins 1998; Fig. 7a):

$$k = 10^{(-20+5.5n)}. \quad (7)$$

Porosity-permeability relationships from a synthesis of data for several subduction margins (Gamage *et al.* 2011) yield similar results. The sediment permeabilities derived from (7) are modified iteratively at each point during the solution to attain a steady-state that is consistent with fluid pressure ratios less than or equal to 1. That is, if fluid pressure exceeds lithostatic pressure, permeability is locally and permanently increased by a small factor (1.05×) to simulate the effects of hydraulic fracturing that would open permeable pathways and limit 'valve' pressures (*cf.* Spinelli *et al.* 2006). Apart from this modification, we do not consider effects of transient changes in permeability (e.g. Bekins *et al.* 1995).

The décollement and slab permeabilities that we use are listed in Table 3. Model F1 uses décollement permeabilities similar to those estimated for other subduction margins, in which the décollement is assumed to have a high permeability underlain by much lower-permeability subducting sediment (Saffer & Bekins 1998; Kukowski & Pecher 1999; Lauer & Saffer 2012). In a sensitivity study of model F1 (not shown), we tested the effect of a high-permeable slab (with a permeability of 10^{-15} m^2) but found that it made little difference provided the slab was not connected by a permeable pathway to the seafloor. This agrees with the model predictions of Spinelli & Harris (2011), who showed that a subducting seamount can have a considerable effect on fluid flow and heatflow seaward of the trench if a permeable pathway links the basaltic crustal aquifer to the overlying ocean, but that this effect is much smaller once the seamount is landward of the trench where such high-permeable pathways are closed.

Model F2 is similar to F1, but tests the effect of low décollement permeability landward of the seamount. Such a low permeability would be appropriate for a clay-dominated shear zone where fracture-related transient permeability is healed over interseismic timescales, resembling the melange shear zones commonly found in exhumed subduction-related rocks from depth (e.g. Fagereng & Sibson 2010). We also tested two variants of model F2 designed to maximise the chances of attaining overpressure in and below the wedge. The first (not shown, as results were similar) had a slab permeability of 10^{-20} m^2; although slab permeabilities may be high in the top-most few hundred metres as discussed above (and e.g. Fisher 1998), some geophysical studies suggest much lower slab permeabilities at depth (e.g. Audet *et al.* 2009). The second variant

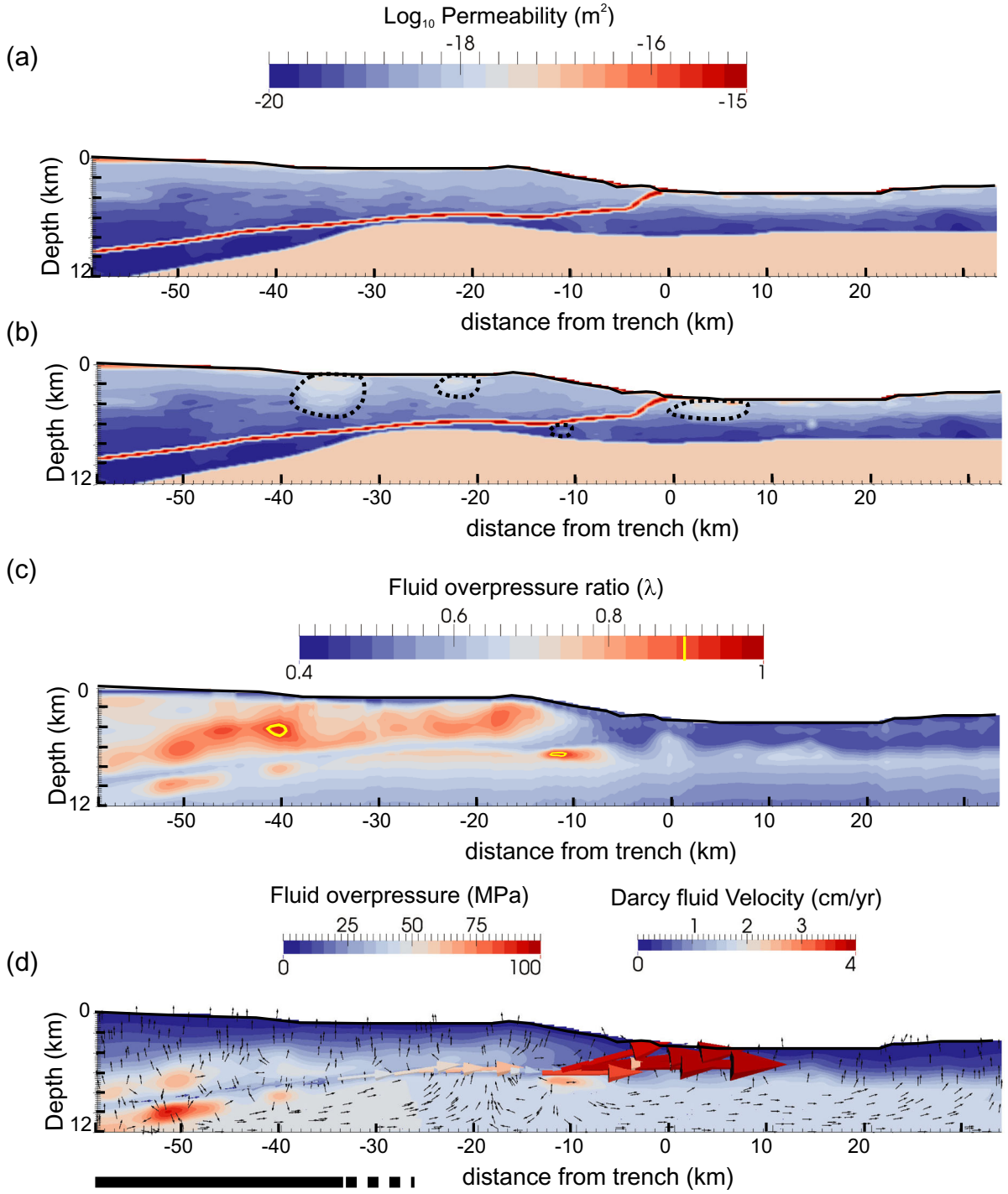

Figure 7. Fluid-flow model F1 as discussed in Section 5. (a) Initial permeability of model. Permeability in wedge and subducted sediment is derived from eq. (7) while a constant permeability of 10^{-15} m^2 along the décollement and 10^{-17} m^2 in oceanic crust and seamount are assumed. (b) Permeability of model F1 adjusted iteratively during transient fluid calculation so that fluid pressure cannot exceed rock pressure (black dashed regions). Décollement and slab permeabilities are not changed. (c) Modified fluid pressure ratio (eq. 1) after model has attained steady-state, where 0.4 is hydrostatic and 1 is lithostatic fluid pressure. Regions with $\lambda \geq 0.9$ are outlined in yellow. (d) Colour plot of excess fluid pressure (above hydrostatic) predicted by the model for steady-state flow. Black vectors show direction of Darcy fluid flow. Coloured vectors are Darcy fluid flow scaled by the magnitude of flow (in cm yr^{-1}, see legend). Black bar at base indicates region of interface inferred to move during slow slip events, which also corresponds to zone of high-amplitude reflectivity on Fig. 1 (Bell *et al.* 2010; Wallace & Beavan 2010).

of model F2 turned off the iterative adjustment of permeability in subducting sediment, as discussed below.

Fig. 7(a) shows the initial permeability for model F1. This permeability was evolved as detailed above to account for effects of hydro-fracturing. After a few steps, this converged to a steady-state solution (Fig. 7b). The zones where permeability was automatically adjusted are outlined with black dashes. Above the seamount, these regions are all located within the wedge (not subducting sediment)

Table 3. Fluid-flow model parameter values.

Model	Décollement permeability (m^2)			Slab permeability (m^2)	Highest fluid overpressure attained in Region IV (λ)	Fig.
	Region IV	Region III	Region I			
F1	10^{-15}	10^{-15}	10^{-15}	10^{-17}	0.8 (0.8)[a]	7
F2	10^{-20}	10^{-15}	10^{-15}	10^{-17}	0.9 (1.0)[a]	8

[a]For model variants where hydrofracturing (opening of permeabilities) was not allowed in subducting sediment.

but two areas of adjustment also occur within the incoming subducting sediment: one directly under the steep frontal thrust, and the other seaward of the trench, in the region where proto-thrusts are observed to form along the Hikurangi wedge (Barnes *et al.* 2010). These areas are generally coincident with local maxima in fluid sources (Fig. 4), and the final steady-state solution is consistent with the idea that in areas of large observed porosity loss (manifested as large source terms), higher permeability is required to accommodate the higher fluid fluxes from dewatering.

To estimate the effect of fluid overpressure on rock strength, in Fig. 7(c) we show the fluid pressure ratio λ corrected for water depth, D (eq. 1; Davis *et al.* 1983). Red shows overpressured areas where the effective strength of sediment is significantly weakened; the yellow contours outline $\lambda > 0.9$. Over most of the wedge and subducting sediment, values of λ are 0.6–0.8, while they are < 0.6 within the more permeable décollement. It must be noted that since λ is a ratio, the subducted sediment landward of the seamount—which has the greatest thickness of sediment above it—can have significant fluid overpressure (>70 MPa) without exceeding lithostatic pressure (Fig. 7d, which also shows how fluid is funnelled along the highly permeable décollement at velocities as high as 4 cm yr^{-1}).

Since grid resolution in the fluid-flow models is 160 m and the strong contrast in material properties at the seafloor is interpolated onto this grid, the predicted overpressure near the seafloor is not well constrained in the models within the top few elements of sediment. For this reason, we do not think our models can be used to estimate likely fluid overpressures that would be encountered while drilling <2 km into the wedge. At greater depths the effects of interpolation and discretisation are relatively minor, so that we can be more confident about fluid pressure predictions for the assumed permeability distribution in Model F1.

Bell *et al.* (2010) proposed that the region of high reflectivity and interface slow-slip landward of the seamount (Fig. 1c) could be explained as the result of near-lithostatic fluid pressures along the interface, with increased fluid pressures associated with ponding of fluids there. We have used our model to test under which circumstances we can attain very high fluid pressures landward of the seamount. We have found two possible fluid-flow scenarios consistent with higher fluid pressure in Region IV. The first is to have greater fluid production in that Region than we have estimated here; if fluid production is doubled (for example by greater sediment thickness and/or initial smectite content), the greatest fluid pressure ratio λ is found there. The second alternative is to have an extremely low décollement permeability; for example, if the décollement lies above the condensed sequence of strongly reflective Late Cretaceous-Early Oligocene (70–32 Ma) sediments (Plaza-Faverola *et al.* 2012) it is possible that the sequence of thin nannofossil chalks and mudstones act as a seal. Décollement permeability may also decrease with increasing temperature, pressure and deformation away from the trench, as sediment compaction and cementation occur, and the onset of pressure solution seals permeable fractures and pore spaces by quartz and calcite (e.g., Moore & Saffer 2001). We explore the 'end-member' effects of this in model F2 (Fig. 8) by reducing the permeability along the décollement to a very low value of 10^{-20} m^2 for calculated temperatures >80 °C. Since fluid is being produced in this region, a transient pulse of fluid pressure exceeding lithostatic values 'opens' regions in the wedge and subducting sediment (Fig. 8a, outlined regions). After some time, steady-state flow is attained, and fluid pressure ratios >0.9 are predicted landward of the seamount (yellow outlined region, Fig. 8b; red overpressured zone, Fig. 8c). This effect is even more marked if the iterative adjustment of permeability is not allowed in subducting sediment; then a small zone with $\lambda > 1$ is predicted, although it is unlikely to be sustained as hydraulically-induced shear failure and/or hydrofracturing that would increase permeability and buffer pore pressure at or below lithostatic would tend to develop under these conditions (Fig. 8d).

6 DISCUSSION

The models we used to predict fluid sources and fluid overpressure contain many assumptions, so that the results are indicative only. We acknowledge that several criticisms can be levelled at our approach. Chief among these are steady-state heat-flow, fluid flow and material advection is unlikely to be valid for a wedge undergoing periodic subduction of seamounts. Episodic seamount subduction will change wedge geometry, taper, incoming sediment thickness and composition, and the relative importance of sediment underplating, accretion and erosion through time. Our method for deriving compaction-related fluid sources also assumes that the porosity derived from the seismic reflection analysis is sufficiently resolved and that this porosity field is stationary with respect to the margin. For the fluid-flow models, the permeabilities we have used in the wedge and subducting sediments are poorly constrained, and the effect of upper plate structure and faults has not been considered. We have also neglected fluids produced at depth from dehydration of the oceanic crust, which may enter the model domain along the inferred high-permeability décollement.

While bearing these limitations clearly in mind, the modelling also provides the best-constrained estimate of fluid budgets to-date for northern Hikurangi. Although the predicted pore pressure at all depths may not be well constrained, the approach is still useful for testing hypotheses about the distribution, magnitude, and underlying drivers of pore pressure, and the relative role of compaction-driven fluid loss vs. dehydration at depths <12 km within underthrust and accreted sediment. We discuss some of these aspects in more detail below.

6.1 Comparison of our results with geophysical evidence for high fluid pressures and low effective stresses along 05CM-04

The fluid-flow models discussed in Section 5 indicate that, unless the deeper parts of the subduction interface act as a barrier to fluid flow, maximum fluid pressure ratios are $0.6 < \lambda < 0.8$ through

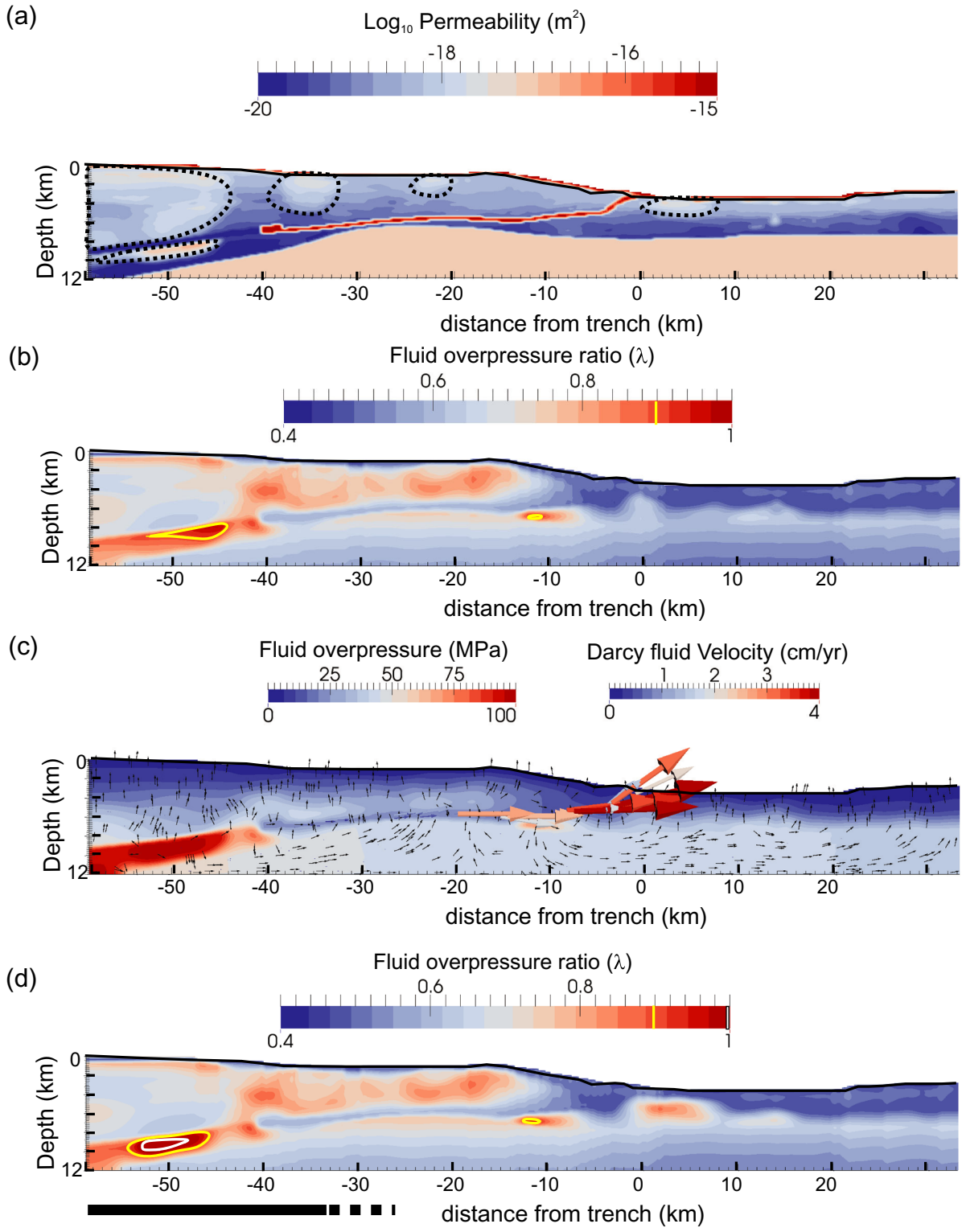

Figure 8. Fluid flow model F2 where décollement has a low permeability for temperatures >80 °C. (a) Final permeability for model F2. Black dashed regions show where permeability has been adjusted to prevent fluid pressure exceeding lithostatic pressure. (b) Fluid overpressure ratio once steady-state has been attained. Regions with $\lambda \geq 0.9$ are outlined in yellow. (c) Colour plot of excess fluid pressure (above hydrostatic) predicted by the model for steady-state flow. Black vectors show direction of Darcy fluid flow. Coloured vectors are Darcy fluid flow scaled by the magnitude of flow. (d) Fluid overpressure ratio for model F2, but where permeabilities have not been adjusted in subducting sediment, so that fluid pressures greater than lithostatic are permitted. Regions with $\lambda \geq 0.9$ are outlined in yellow and those with $\lambda \geq 1$ in white. Black bar at base is region of interface slow slip and high-amplitude reflectivity.

most of the wedge and subducting sediment. We assumed $\lambda = 0.65$ during our initial mechanical calculations (Table 1). To produce wedge mechanics broadly consistent with models of the long-term subduction of a seamount (Electronic Supplement 4) we require quite low effective friction coefficients along the décollement. These low friction values give basal shear stresses increasing from 0 MPa (at the toe), to *ca*. 10 MPa beneath the steep frontal wedge, and up to 20 MPa above and landward of the seamount.

The prediction of moderately overpressured fluids and a weak basal décollement agrees with previous estimates of fluid pressures above hydrostatic for the northern Hikurangi margin (Sibson & Rowland 2003). Seismic velocity ratios *Vp*/*Vs* and *P*-wave attenuation values are suggestive of overpressured sediments along the interface (Eberhart-Phillips *et al.* 2005, 2008; Reyners *et al.* 2006; Bassett *et al.* 2014), but also a relatively dry, permeable hanging wall (Eberhart-Phillips *et al.* 2008; Reyners & Eberhart-Phillips 2009). Aqueous fluids emerging in the Northern Hikurangi forearc have mantle/slab He isotope ratios that indicate a permeable upper plate (Reyes *et al.* 2010). This is consistent with sublithostatic fluid pressures, although the warm springs from which the fluid chemistry was derived are further landward and south of the modelled section (Fig. 1).

Bassett *et al.* (2014) used *Vp* ratios derived from refracted arrivals (Fig. 2) to directly derive effective stress (e.g. Moore & Tobin 1997; Kitajima & Saffer 2012), assuming that the northern Hikurangi margin wedge is close to extensional failure whereas the southern margin is close to compressional failure. From this analysis they estimated fluid pressure ratios of around 0.5–0.67 in the north, and as high as 0.87 for southern Hikurangi. Their extensional wedge solutions for northern Hikurangi predicted low basal shear stress values along the décollement (<10 MPa), slightly lower than our estimates, based on modelling and wedge mechanics.

Fagereng & Ellis (2009) computed strength profiles along the subduction interface for northern and southern Hikurangi. For a geothermal gradient along the subduction interface of *ca*. 13 $^{\circ}$C km^{-1} (Fig. 4b), the onset of crystalline plasticity in quartz at 300–350 $^{\circ}$C occurs at about 23–27 km depth. Fagereng & Ellis (2009) computed a shallower brittle–ductile transition than this in the north because they used a high interface friction coefficient of 0.6 and hydrostatic fluid pressure ($\lambda = 0.4$), leading to a frictionally stronger subduction interface there.

With the low basal friction coefficient of ∼0.15 we used here, and fluid pressure ratios of ∼0.6 along the subduction interface, we cannot explain the onset of slow-slip at ∼10 km depth by dislocation creep mechanisms in quartz-controlled crystalline plasticity. Alternative mechanisms include: (1) elevated fluid pressures landward of the seamount along the subduction interface, possibly owing to rapid sealing of the permeable décollement with increasing temperature and clay deformation (e.g. Fig. 8; Kodaira *et al.* 2004; Bell *et al.* 2010); and/or (2) aseismic and/or transient creep mechanisms occur along the subduction interface at temperatures below the commonly accepted lower limit of *ca*. 300–350 $^{\circ}$C. Low-temperature aseismic creep may be aided by subduction of rough seafloor, which will broaden the deforming shear zone to a distributed zone of fractured rocks that deform aseismically by mixed continuous-discontinous shear (e.g. Fagereng & Harris 2014; Wang & Bilek 2014). In fact it is possible that both of these mechanisms operate in tandem, since the second mechanism is aided by locally high fluid pressures. In any case, sufficient permeability must exist across the subduction interface to explain mantle He signature fluids arriving at the surface (Reyes *et al.* 2010); this suggests that the fluid pressure distribution shown in Fig. 7 (model F1) is more likely than that in Fig. 8 (model F2), though it is possible than transient pulses of higher fluid pressure do occur along the interface as shown in Fig. 8.

Bell *et al.* (2010) proposed that the seamount may act as a barrier to fluid flow along the décollement, promoting fluid 'ponding' and high overpressures in the region of slow-slip and enhanced seismic reflectivity there. We have found through sensitivity tests that cutting off a small region of the permeable décollement above the seamount does not produce high fluid pressures in the sediment package landward of it. A continuous, low-permeability seal is required above subducting sediment to prevent fluids escaping to the wedge (e.g., Fig. 8). In three dimensions, if the seamount were acting as a fluid-flow barrier, fluid would be expected to flow around it; this effect remains to be tested in future (3D) models. However, based on our results we think that the main effects of the seamount are: (1) to allow a significantly thick package of fluid-rich sediment to subduct to depth below the wedge, such that pore fluids are subducted deeper than, for example, in Nankai and (2) to transiently perturb deformation along the subduction interface and within the wedge, increasing the complexity and roughness of the interface in the manner outlined by Wang & Bilek (2014).

6.2 Why are porosities maintained in the wedge?

The seismic reflection analysis along line 05CM-04 indicates a negligible reduction in porosity as material accretes from incoming sediment into the wedge or is subducted beneath it (Fig. 2a). One explanation for the maintenance of relatively high porosity is that the sediments are undercompacted (where undercompaction means greater porosity at depth than is typical for other subduction margins). This can occur if cementation prevents pores from closing with increased overburden pressure, or via severe disequilibrium compaction with essentially undrained behaviour and high pore pressures. The latter mechanism is enhanced by high sedimentation rates and is likely to be limited in depth.

Bassett *et al.* (2014) suggest that high fluid pressures can lead to apparent high porosity in accreting and subducting material in northern Hikurangi by promoting pervasive fracturing. However, fracture-related secondary porosity will also increase the permeability of the wedge, for example along continuous fractures and faults to the seafloor. In fact, our fluid flow models in Section 5 require some increase in wedge permeability to avoid overpressures near the prism toe (Fig. 7b), although we do not model the interaction with wedge mechanics during this process. Increased wedge permeability through a fracture system reduces fluid overpressure to moderate (sublithostatic) values in the wedge above the subducted sediments, although locally higher fluid pressures may occur within the underthrust sediments provided they are hydraulically sealed from the overlying wedge (e.g. Fig. 8).

An additional tectonic factor may help account for the lack in consolidation: that fracture-related secondary deformation occurs as the wedge transiently adjusts to the passage of seamounts with cycles of frontal and basal erosion and accretion (Fig. ES4; Collot *et al.* 1996, 2001). This could also explain the particularly high porosities near the toe of the wedge.

6.3 Clay dehydration: comparison with geophysics, and effect on fault friction

The models predict that clay dehydration is a significant source of fluid starting at depths of around 10 km, *ca*. 40 km landward of the trench. This depth corresponds roughly to a change from

electrically conductive to less conductive material just above the subducting plate imaged in a recent magnetotelluric study (Heise *et al.* 2013). Our models support the conjecture of Heise *et al.* (2013) that this change is related to the transition from conductive smectite to less conductive illite. The modelled clay dehydration in the subducting sediment shown in Fig. 4(b) coincides with a highly reflective zone imaged by Bell *et al.* (2010) that they ascribed to high fluid pressures. Is this reflectivity caused by high fluid pressures alone, or could it be partly related to an intrinsic property of the clay mineralogy as it changes with depth? These effects are difficult to separate, because the smectite to illite transition both changes the clay mineralogy and releases water, so that a combination of changes in fluid content and mineralogy is likely in this zone.

The transition from smecite to illite may also have consequences for frictional behaviour of the interface. Water-saturated smectite has been measured to have friction coefficients as low as 0.1 (Moore & Lockner 2007), sufficiently low to be consistent with the low frictional coefficients required by our sensitivity analyses. Saffer & Marone (2003) measured an increase in frictional strength from smectite (0.15–0.32) to illite (0.42–0.68) and found that illite was velocity-strengthening at all measured normal stresses, consistent with aseismic slip, whereas smectite was velocity-weakening at low effective normal stresses. It is therefore possible that the change from smectite to illite is at least partially responsible for the downdip change from locked to creeping in this part of the Hikurangi margin.

6.4 What are the mechanical properties of the décollement at depth?

Although we have modelled the subduction interface as a narrow décollement to 12 km depth, if it is permeable it will have a lower fluid pressure than underlying sediment, especially landward of the seamount (Fig. 7). This reduces the likelihood that the interface continues as a narrow shear zone, since sediment beneath it will be frictionally weakened by having lower effective stresses; instead, the locus of deformation may widen and transiently shift across a broad sheared melange, as is seen in some exhumed examples interpreted as ancient subduction interfaces (e.g. Fagereng & Sibson 2010). Such widening agrees with Rowe *et al.*'s (2013) model of a thick subduction thrust interface based on drill cores and exhumed subduction thrust interfaces from a range of locations and representing depths down to ∼15 km. In their model, the actively deforming subduction thrust is a zone hundreds of metres wide, containing several thin, discrete fault surfaces. For our fluid flow models, a wide interface internal structure implies that permeability is likely to be maintained along discrete, interface-parallel surfaces, although the active slip surface may be transient and move with time within a thicker zone of deforming subducting sediments. However, this model also implies an interplay between frictional sliding on discrete slip surfaces, and distributed deformation by dissolution-precipitation creep in surrounding sediments (e.g. Fagereng 2011a), at least at depths where temperatures are conducive to pressure solution in quartz (Moore *et al.* 2007). Competition between frictional sliding and dissolution–precipitation creep is likely modulated by fluid pressure, where elevated fluid pressure would reduce frictional strength and promote frictional sliding, and the relative importance may vary in time as a function of fluid pressure transients. The increased fluid release downdip of the seamount may promote either dissolution precipitation, in the case of high permeability, or frictional sliding, if permeability is low.

Alternatively, the interface may be located along or just above the condensed sequence of Late Cretaceous–Early Oligocene chalks and mudstones, or along an overpressured clay gouge horizon with low permeability (e.g., Fig. 8). In this case, it may be a narrow zone above the seamount, and continue as a narrow zone to depth, because low friction clays combined with localized high fluid pressure can maintain such a horizon as a weak, preferred plane of failure (Moore & Lockner 2007). The subducted sediments below the décollement are still likely to be fluid-saturated and fine-grained, and conducive to interseismic distributed deformation by dissolution-precipitation creep or distributed cataclasis (e.g. Gratier *et al.* 2013). However, in this model, the subduction thrust would contain a single discrete slip surface above the subducting sediments, rather than numerous faults within a thicker deforming zone. Overall, this is not our preferred model, as fluid chemistry reported by Reyes *et al.* (2010) indicates at least transient permeability where the surface is connected to the mantle. Also, discrete slip surfaces within or above dehydrating subducting sediments are likely to be sealed by quartz and/or calcite cements precipitated from hydrothermal fluids along the impermeable horizon, for example as fluid pressure fluctuates associated with episodic slip along the subduction interface (e.g. Sibson 1996). Such fault sealing is likely to strengthen the slip surface, and promote generation of new slip surfaces within the subducting sediments, for example along cleavage or relict bedding, rather than reshear of the sealed horizon (Fagereng 2011b).

6.5 Effect of splay faults in upper plate

We have not modelled development of secondary splay faults in the wedge, since our models are 'snapshots' in time starting from the present-day geometry and geophysics. Lauer & Saffer (2012) investigated the effect that permeable faults in the wedge can have on décollement overpressures for the Costa Rican subduction margin. They found that permeable splay faults can significantly affect the geochemistry and geophysics of the subduction margin, accounting for between 6 and 35 per cent of the total dewatering of sediment. They assumed splay fault permeabilities of between 10^{-16} m^2 and 10^{-13} m^2, which are significantly higher permeabilities than those we derived for the wedge from eq. (7). The iterative increase in permeabilities we used to prevent fluid pressure ratios >1 in some ways simulate the effect and opening of permeable pathways along splay faults, though they are purely fluid-controlled (Figs 7 and 8). We found that we needed to iteratively increase permeabilities by an order of magnitude in the wedge to prevent unphysical fluid pressures. These regions were spread over a broad zone; if taken up along a narrow splay fault, this would require even greater increases in permeability, consistent with the findings of Lauer & Saffer (2012).

6.6 Influence of seamount subduction on fluid generation and overpressure

Based on the results shown here, we think that the main effect of the subducting seamount imaged on line 05CM-04 is to have facilitated the local underplating of a thick layer of sediment beneath the wedge. This sediment package acts as a reservoir for compaction- and dehydration fluid release at depth, causing elevated fluid pressures and a change in clay mineralogy immediately landward of the seamount in its current location. If the seamount also causes a significant reduction in decollement permeability, by decreasing the thickness of the subducting sediment layer or impinging directly on the crystalline hanging wall, it may act as a barrier to fluid flow, possibly enhancing overpressure. If, on the other hand, the seamount is a zone of increased fracture intensity (Wang & Bilek 2014), it is

possible that it represents a zone of elevated fracture permeability and connectivity of fluid pathways from the subducting sediments into the wedge. In this latter case, fluid overpressures may not be as high as predicted in Figs 7 and 8. Thus, although we predict significantly elevated fluid release along the subduction interface downdip of the seamount, the overall effect of the seamount on permeability, and therefore the effect on fluid pressure, remains uncertain.

6.7 Consistency of the mechanical model in Section 4 and fluid overpressure predictions from Section 5

Sections 4 and 5 separate out models of the mechanical and fluid-flow steady-states for the wedge and subducting sediment in order to demonstrate the different controls on the system. A progressive iteration of mechanical strength and fluid pressure starting from the present-day wedge bathymetry is non-unique and develops instabilities, since fluid pressures are initially not in balance, creating transient mechanical behaviour.

However, we performed a simple check to make sure that mechanical and fluid-flow models are broadly consistent with each other, using results from the fluid flow model (F1) at steady-state, where fluid pressures had reached equilibrium and permeability had evolved to prevent supra-lithostatic values (Fig. 7b). We used the fluid pressure ratio λ, from Fig. 7(c) as input to the mechanical model and recomputed the material flow and predicted volumetric fluid production from the porosity field. We found that the mechanical model predicted similar wedge dynamics to that shown in Fig. 3(b), and that predicted fluid release from compaction in the wedge and subducted sediment differed by <10 per cent from the values listed in Table 2. A further improvement to the models shown here would be to iterate several times back and forth between mechanics and fluid-flow, but we do not think it would change results significantly, provided the initial (dry) friction values used in the mechanical model are sufficiently strong, as in Table 1.

7 CONCLUSIONS

We have used a 2-D thermomechanical-fluid model to estimate fluid overpressure for a profile along the northern Hikurangi subduction margin. The results show that:

(1) The northern Hikurangi margin has relatively small rates of fluid production in the wedge compared to previous (average) estimates for the margin and other subduction margins (Table 2), because the persistence of high porosity across the wedge retains fluid in the system. Fluid is released by compaction mainly in the subducting sediment seaward and landward of a subducting seamount, and beneath the steep frontal wedge.

(2) The models predict that clay dehydration reactions produce fluid in the subducting sediment starting at depths of around 10 km, *ca*. 40 km landward of the trench, although volumetric fluid production rates are an order of magnitude less than those from porosity loss.

(3) Based on the model results, we think that the main effect of a subducting seamount on fluid sources and overpressure is to enhance the subduction of thick packets of sediment to depth. Overpressures are predicted landward of the seamount in the subducting sediment. This location corresponds to the high reflectivity zone imaged on line 05CM-04 by Bell *et al.* (2010). This spatial coincidence is compatible with moderately high fluid pressure affecting the enhanced reflectivity, but it could also be related to changes in mechanical properties of the subduction interface there, particularly the change in clay mineralogy.

(4) Fluid overpressure is likely within the northern Hikurangi profile, although we do not predict that substantial parts of the wedge or subducting sediment remain at or near lithostatic fluid pressure values. Our simple fluid-flow model shows that fluid overpressure is most likely to be retained within the subducting sediment on either side of the seamount. Changes in permeability from hydrofracturing are predicted within the wedge, providing permeable pathways for fluids to the surface, and seaward of the wedge in the proto-thrust region. More significant overpressures, with fluid pressure ratios of 0.95 or higher, may develop along the subduction interface landward of the seamount if a thin, extremely low-permeability seal is present along the décollement there.

(5) In the future, more detailed analyses constraining rates of fluid expulsion along faults and seeps using fluid chemistry and residence times will improve fluid budget estimates and determination of fluid overpressure with depth.

ACKNOWLEDGEMENTS

This work was supported by a combination of Marsden grants GNS1204 (Ellis) and GNS0902 (Henrys, Williams), and Direct Core Funding to GNS Science through the 'Tectonics of Zealandia' programme. The code *SULEC* was jointly written by Susan Ellis and Susanne Buiter. We acknowledge useful discussions with Phil Barnes, Francesca Ghisetti, Katrina Marson-Pidgeon, Susanne Buiter, Rachel Lauer, Harold Tobin, Rupert Sutherland, Rebecca Bell, John Townend, Ingo Pecher, and Gareth Crutchley. Nathan Bangs helped with the PDMA analysis discussed in Electronic Supplement 1. We thank the two anonymous reviewers for their constructive and detailed comments on the manuscript.

REFERENCES

Audet, P., Bostock, M.G., Christensen, N.I. & Peacock, S.M., 2009. Seismic evidence for overpressured subducted oceanic crust and megathrust fault sealing, *Nature,* **457**(7225), 76–78

Barker, D.H., Sutherland, R., Henrys, S. & Bannister, S., 2009. Geometry of the Hikurangi subduction thrust and upper plate, North Island, New Zealand, *Geochem. Geophys. Geosyst.,* **10,** doi:10.1029/2008GC002153.

Barnes, P.M. *et al.*, 2010. Tectonic and geological framework for gas hydrates and cold seeps on the Hikurangi subduction margin, New Zealand, *Mar. Geol.,* **272,** 26–48.

Bassett, D., Sutherland, R. & Henrys, S., 2014. Slow wavespeeds and fluid overpressure in a region of shallow geodetic locking and slow slip, Hikurangi subduction margin, New Zealand, *Earth planet. Sci. Lett.,* **389,** 1–13.

Beavan, J., Tregoning, P., Bevis, M., Kato, T. & Meertens, C., 2002, Motion and rigidity of the Pacific Plate and implications for plate boundary deformation, *J. geophys. Res.: Solid Earth (1978–2012),* **107**(B10), 2261, doi:10.1029/2001JB000282.

Becker, K., Fisher, A. & Davis, E., 1997. The CORK experiment in Hole 949C: long-term observations of pressure and temperature in the Barbados accretionary prism, in *Proceedings of the Ocean Drilling Program,* Scientific results, pp. 247–252, Ocean Drilling Program.

Bekins, B.A. & Dreiss, S.J., 1992. A simplified analysis of parameters controlling dewatering in accretionary prisms, *Earth planet. Sci. Lett.,* **109,** 275–287.

Bekins, B.A., McCaffrey, A.M. & Dreiss, S.J., 1995. Episodic and constant flow models for the origin of low-chloride waters in a modern accretionary prism, *Water Resour. Res.,* **31,** 3205–3215.

Bell, R., Sutherland, R., Barker, D.H., Henrys, S., Bannister, S., Wallace, L. & Beavan, J., 2010. Seismic reflection character of the Hikurangi subduction interface, New Zealand, in the region of repeated Gisborne slow slip events, *Geophys. J. Int.,* **180,** 34–48.

Bethke, C.M., 1986. Inverse hydrologic analysis of the distribution and origin of Gulf Coast-type geopressured zones, *J. geophys. Res.: Solid Earth,* **91,** 6535–6545.

Bray, C. & Karig, D., 1985. Porosity of sediments in accretionary prisms and some implications for dewatering processes, *J. geophys. Res.: Solid Earth (1978–2012),* **90,** 768–778.

Brocher, T.M., 2005. Empirical relations between elastic wavespeeds and density in the Earth's crust, *Bull. seism. Soc. Am.,* **95,** 2081–2092.

Buiter, S. & Ellis, S., 2012. Benchmarking a new ALE finite-element code, in *Geophysical Research Abstracts,* Vol. 14, EGU.

Byrne, T. & Fisher, D., 1990. Evidence for a weak and overpressured décollement beneath sediment-dominated accretionary prisms, *J. geophys. Res.: Solid Earth,* **95,** 9081–9097.

Calahorrano, B.A., Sallarès, V., Collot, J.-Y., Sage, F. & Ranero, C.R., 2008. Nonlinear variations of the physical properties along the southern Ecuador subduction channel: results from depth-migrated seismic data, *Earth planet. Sci. Lett.,* **267,** 453–467.

Collot, J.-Y. *et al.*, 1996. From oblique subduction to intra-continental transpression: structures of the southern Kermadec-Hikurangi margin from multibeam bathymetry, side-scan sonar and seismic reflection, *Marine. Geophys. Res.,* **18,** 357–381.

Collot, J.Y., Lewis, K., Lamarche, G. & Lallemand, S., 2001. The giant Ruatoria debris avalanche on the northern Hikurangi margin, New Zealand: result of oblique seamount subduction, *J. geophys. Res.: Solid Earth (1978–2012),* **106,** 19 271–19 297.

Colten-Bradley, V.A., 1987. Role of pressure in smectite dehydration–effects on geopressure and smectite-to-illite transformation, *AAPG Bull.,* **71,** 1414–1427.

Dahlen, F., 1984. Noncohesive critical Coulomb wedges: an exact solution, *J. geophys. Res.: Solid Earth (1978–2012),* **89,** 10 125–10 133.

Dahlen, F., 1990. Critical taper model of fold-and-thrust belts and accretionary wedges, *Ann. Rev. Earth planet. Sci.,* **18,** 55–99.

Dahlen, F., Suppe, J. & Davis, D., 1984. Mechanics of fold-and-thrust belts and accretionary wedges: cohesive Coulomb theory, *J. geophys. Res.: Solid Earth (1978–2012),* **89,** 10 087–10 101.

Davis, D., Suppe, J. & Dahlen, F., 1983. Mechanics of fold-and-thrust belts and accretionary wedges, *J. geophys. Res.: Solid Earth (1978–2012),* **88,** 1153–1172.

Davy, B. & Wood, R., 1994. Gravity and magnetic modelling of the Hikurangi Plateau, *Mar. Geol.,* **118,** 139–151.

Davy, B., Hoernle, K. & Werner, R., 2008. Hikurangi Plateau: crustal structure, rifted formation, and Gondwana subduction history, *Geochem. Geophys. Geosyst.,* **9**.

Dominguez, S., Malavieille, J. & Lallemand, S.E., 2000. Deformation of accretionary wedges in response to seamount subduction: Insights from sandbox experiments, *Tectonics,* **19**(1), 182–196.

Doser, D.I. & Webb, T.H., 2003, Source parameters of large historical (1917–1961) earthquakes, North Island, New Zealand, *Geophys. J. Int.,* **152**(3), 795–832.

Eberhart-Phillips, D., Reyners, M., Chadwick, M. & Chiu, J.M., 2005. Crustal heterogeneity and subduction processes: 3-D Vp, Vp/Vs and Q in the southern North Island, New Zealand, *Geophys. J. Int.,* **162,** 270–288.

Eberhart-Phillips, D., Reyners, M., Chadwick, M. & Stuart, G., 2008. Three-dimensional attenuation structure of the Hikurangi subduction zone in the central North Island, New Zealand, *Geophys. J. Int.,* **174,** 418–434.

Ellis, S., Little, T., Wallace, L., Hacker, B. & Buiter, S., 2011. Feedback between rifting and diapirism can exhume ultrahigh-pressure rocks, *Earth planet. Sci. Lett.,* **311,** 427–438.

Erickson, S.N. & Jarrard, R.D., 1998. Velocity-porosity relationships for water-saturated siliciclastic sediments, *J. geophys. Res.: Solid Earth (1978–2012),* **103,** 30 385–30 406.

Ernst, W. & Calvert, S., 1969. An experimental study of the recrystallization of porcelanite and its bearing on the origin of some bedded cherts, *Am. J. Sci.,* **267,** 114–133.

Fagereng, Å., 2011a. Geology of the seismogenic subduction thrust interface, in *Geology of the Earthquake Source: A Volume in Honour of Rick Sibson,* Vol. 359, pp. 55–76, eds Fagereng, A., Toy, V.G. & Rowland, J.V., Geological Society, Special Publications.

Fagereng, Å., 2011b. Fractal vein distributions within a fault-fracture mesh in an exhumed accretionary melange, Chrystalls Beach Complex, New Zealand, *J. Struct. Geol.,* **33,** 918–927.

Fagereng, Å. & Diener, J.F., 2011. Non-volcanic tremor and discontinuous slab dehydration, *Geophys. Res. Lett.,* **38**, L15302, doi:10.1029/2011GL048214.

Fagereng, Å. & Ellis, S., 2009. On factors controlling the depth of interseismic coupling on the Hikurangi subduction interface, New Zealand, *Earth planet. Sci. Lett.,* **278,** 120–130.

Fagereng, Å. & Harris, C., 2014. Interplay between fluid flow and fault–fracture mesh generation within underthrust sediments: geochemical evidence from the Chrystalls Beach Complex, New Zealand, *Tectonophysics,* **612,** 147–157.

Fagereng, Å. & Sibson, R.H., 2010. Melange rheology and seismic style, *Geology,* **38,** 751–754.

Field, B.D. *et al.*, 1997. Cretaceous-Cenozoic geology and petroleum systems of the East Coast Region, New Zealand, in *Institute of Geological and Nuclear Sciences Monograph,* Vol. 19, pp. 301, 7 enclosures, Lower Hutt, New Zealand: Institute of Geological & Nuclear Sciences Limited.

Fisher, A.T., 1998. Permeability within basaltic oceanic crust, *Rev. Geophys.,* **36,** 143–182.

Fitts, T.G. & Brown, K.M., 1999. Stress-induced smectite dehydration: ramifications for patterns of freshening and fluid expulsion in the N. Barbados accretionary wedge, *Earth planet. Sci. Lett.,* **172**(1), 179–197.

Gamage, K., Screaton, E., Bekins, B. & Aiello, I., 2011, Permeability–porosity relationships of subduction zone sediments, *Mar. Geol.,* **279**(1), 19–36.

Gardner, G., Gardner, L. & Gregory, A., 1974. Formation velocity and density-the diagnostic basics for stratigraphic traps, *Geophysics,* **39**(6), 770–780.

Gettemy, G.L., Tobin, H.J., Hole, J.A. & Sayed, A.Y., 2004. Multi-scale compressional wave velocity structure of the San Gregorio Fault zone, *Geophys. Res. Lett.,* **31,** L06601, doi:10.1029/2003GL018826.

Gratier, J.P., Dysthe, D. & Renard, F., 2013. The role of pressure solution creep in the ductility of the Earth's upper crust, *Adv. Geophys.,* **54,** doi:10.1016/B978-0-12-380940-7.00002-0.

Hacker, B.R., Abers, G.A. & Peacock, S.M., 2003. Subduction factory 1. Theoretical mineralogy, densities, seismic wave speeds, and H_2O contents, *J. geophys. Res.: Solid Earth (1978–2012),* **108,** doi:10.1029/2001JB001127.

Heise, W., Caldwell, T.G., Bertrand, E.A., Hill, G.J., Bennie, S.L. & Ogawa, Y., 2013. Changes in electrical resistivity track changes in tectonic plate coupling, *Geophys. Res. Lett.,* **40,** 5029–5033.

Henrys, S., Reyners, M., Pecher, I., Bannister, S., Nishimura, Y. & Maslen, G., 2006. Kinking of the subducting slab by escalator normal faulting beneath the North Island of New Zealand, *Geology,* **34,** 777–780.

Henrys, S.A., Ellis, S. & Uruski, C., 2003. Conductive heat flow variations from bottom-simulating reflectors on the Hikurangi margin, New Zealand, *Geophys. Res. Lett.,* **30,** doi:10.1029/2002GL015772.

Hensen, C., Wallmann, K., Schmidt, M., Ranero, C.R. & Suess, E., 2004. Fluid expulsion related to mud extrusion off Costa Rica—a window to the subducting slab, *Geology,* **32,** 201–204.

Hillier, S., 1993. Origin, diagenesis, and mineralogy of chlorite minerals in Devonian lacustrine mudrocks, Orcadian basin, Scotland, *Clays Clay Miner.,* **41,** 240–259.

Hoernle, K., Hauff, F., Van den Bogaard, P., Werner, R., Mortimer, N., Geldmacher, J., Garbe-Schönberg, D. & Davy, B., 2010. Age and geochemistry of volcanic rocks from the Hikurangi and Manihiki oceanic plateaus, *Geochim. Cosmochim. Acta,* **74,** 7196–7219.

Hoffman, N.W. & Tobin, H.J., 2004. An empirical relationship between velocity and porosity for underthrust sediments in the Nankai Trough accretionary prism, in *Proceedimgs of the ODP, Sci. Results,* Vol. 190/196, eds Mikada, H., Moore, G.F., Taira, A., Becker, K., Moore, J.C. & Klaus, A., http://www-odp.tamu.edu/publications/190196SR/355/355.htm, last accessed 2 April 2015.

Hubbert, M.K. & Rubey, W.W., 1959. Role of fluid pressure in mechanics of overthrust faulting, 1. Mechanics of fluid-filled porous solids and its application to overthrust faulting, *Bull. geol. Soc. Am.,* **70,** 115–166.

Kameda, J., Yamaguchi, A., Saito, S., Sakuma, H., Kawamura, K. & Kimura, G., 2011. A new source of water in seismogenic subduction zones, *Geophys. Res. Lett.,* **38,** L22306, doi:10.1029/2011GL048883.

Kastner, M., Elderfield, H. & Martin, J., 1991. Fluids in convergent margins: what do we know about their composition, origin, role in diagenesis and importance for oceanic chemical fluxes?, *Phil. Trans. R. Soc. Lond. Ser. A: Phys. Eng. Sci.,* **335,** 243–259.

Kerrick, D.M. & Connolly, J.A.D., 2001. Metamorphic devolatilization of subducted oceanic metabasalts: implications for seismicity, arc magmatism, and volatile recycling, *Earth planet. Sci. Lett.,* **189,** 19–29.

Kitajima, H. & Saffer, D.M., 2012. Elevated pore pressure and anomalously low stress in regions of low frequency earthquakes along the Nankai Trough subduction megathrust, *Geophys. Res. Lett.,* **39**, L23301, doi:10.1029/2012GL053793.

Kodaira, S., Iidaka, T., Kato, A., Park, J.-O., Iwasaki, T. & Kaneda, Y., 2004. High pore fluid pressure may cause silent slip in the Nankai Trough, *Science,* **304,** 1295–1298.

Kukowski, N. & Pecher, I., 1999. Thermo-hydraulics of the Peruvian accretionary complex at 12°S, *J. Geodyn.,* **27,** 373–402.

Lauer, R.M. & Saffer, D.M., 2012. Fluid budgets of subduction zone forearcs: the contribution of splay faults, *Geophys. Res. Lett.,* **39**, L13604, doi:10.1029/2012GL052182.

Lewis, K. & Pettinga, J., 1993. The emerging, imbricate frontal wedge of the Hikurangi margin, *Sediment. Basins World,* **2,** 225–250.

Lewis, K.B., Collot, J.Y. & Lallem, S.E., 1998. The dammed Hikurangi Trough: a channel-fed trench blocked by subducting seamounts and their wake avalanches (New Zealand–France GeodyNZ Project), *Basin Res.,* **10,** 441–468.

Liu, Y. & Rice, J.R., 2005. Aseismic slip transients emerge spontaneously in three-dimensional rate and state modeling of subduction earthquake sequences, *J. geophys. Res.: Solid Earth (1978–2012),* **110,** doi:10.1029/2004JB003424.

Liu, Y. & Rice, J.R., 2007. Spontaneous and triggered aseismic deformation transients in a subduction fault model, *J. geophys. Res.: Solid Earth (1978–2012),* **112,** doi:10.1029/2007JB004930.

Matmon, D. & Bekins, B.A., 2006. Hydromechanics of a high taper angle, low-permeability prism: a case study from Peru, *J. geophys. Res.: Solid Earth (1978–2012),* **111,** B07101, doi:10.1029/2005JB003697.

Moore, J.C. & Tobin, H.J., 1997. Estimated fluid pressures of the Barbados accretionary prism and adjacent sediments, in *Proceedings of the ODP, Scientific Results,* **Vol. 156,** pp. 229–238, eds Shipley, T.H., Ogawa, Y., Blum, P. & Bahr, J.M., et al., College Station, TX (Ocean Drilling Program).

Moore, D.E. & Lockner, D.A., 2007. Friction of the smectite clay montmorillonite. in *The Seismogenic Zone of Subduction Thrust Faults,* pp. 317–345, eds Dixon, T.H. & Moore, J.C., Columbia University Press.

Moore, J.C. & Saffer, D., 2001, Updip limit of the seismogenic zone beneath the accretionary prism of southwest Japan: an effect of diagenetic to low-grade metamorphic processes and increasing effective stress, *Geology,* **29**(2), 183–186.

Moore, J.C., Rowe, C. & Meneghini, F., 2007, How Accretionary Prisms Elucidate Seismogenesis in Subduction Zones, in *The Seismogenic Zone of Subduction Thrust Faults*, pp. 288–315, eds Dixon, T.H. & Moore, J.C., Columbia University Press.

Moore, G.F. *et al.*, 2001. New insights into deformation and fluid flow processes in the Nankai Trough accretionary prism: results of Ocean Drilling Program Leg 190, *Geochem. Geophys. Geosyst.,* **2,** doi:10.1029/2001GC000166.

Moore, G.F., Saffer, D., Studer, M. & Costa Pisani, P., 2011. Structural restoration of thrusts at the toe of the Nankai Trough accretionary prism off Shikoku Island, Japan: implications for dewatering processes, *Geochem. Geophys. Geosyst.,* **12,** Q0AD12, doi:10.1029/2010GC003453.

Morgan, J. & Karig, D., 1995. Kinematics and a balanced and restored cross-section across the toe of the eastern Nankai accretionary prism, *J. Struct. Geol.,* **17,** 31–45.

Mortimer, N. & Parkinson, D., 1996. Hikurangi Plateau: a Cretaceous large igneous province in the southwest Pacific Ocean, *J. geophys. Res.: Solid Earth (1978–2012),* **101,** 687–696.

Neuzil, C., 1995. Abnormal pressures as hydrodynamic phenomena, *Am. J. Sci.,* **295,** 742–786.

Pecher, I.A. *et al.*, 2010. Focussed fluid flow on the Hikurangi Margin, New Zealand—evidence from possible local upwarping of the base of gas hydrate stability, *Mar. Geol.,* **272,** 99–113.

Pedley, K.L., Barnes, P.M., Pettinga, J.R. & Lewis, K.B., 2010. Seafloor structural geomorphic evolution of the accretionary frontal wedge in response to seamount subduction, Poverty Indentation, New Zealand, *Mar. Geol.,* **270,** 119–138.

Plaza-Faverola, A., Klaeschen, D., Barnes, P., Pecher, I., Henrys, S. & Mountjoy, J., 2012. Evolution of fluid expulsion and concentrated hydrate zones across the southern Hikurangi subduction margin, New Zealand: an analysis from depth migrated seismic data, *Geochem. Geophys. Geosyst.,* **13,** doi:10.1029/2012GC004228.

Pytte, A. & Reynolds, R., 1988. The thermal transformation of smectite to illite, in *Thermal Histories of Sedimentary Basins,* pp. 133–140, eds Naeser, N.D. & McCulloh, T.H., Springer-Verlag.

Reyes, A., Christenson, B. & Faure, K., 2010. Sources of solutes and heat in low-enthalpy mineral waters and their relation to tectonic setting, New Zealand, *J. Volc. Geotherm. Res.,* **192,** 117–141.

Reyners, M. & Eberhart-Phillips, D., 2009. Small earthquakes provide insight into plate coupling and fluid distribution in the Hikurangi subduction zone, New Zealand, *Earth planet. Sci. Lett.*, **282**(1), 299–305.

Reyners, M., Eberhart-Phillips, D., Stuart, G. & Nishimura, Y., 2006. Imaging subduction from the trench to 300 km depth beneath the central North Island, New Zealand, with Vp and Vp/Vs, *Geophys. J. Int.,* **165,** 565–583.

Ridgway, N.M., 1969. Temperature and salinity of sea water at the ocean floor in the New Zealand region, *N. Z. J. Mar. Freshwater Res.,* **3**(1), 57–72.

Rowe, C.D., Moore, J.C. & Remitti, F., 2013. The thickness of subduction plate boundary faults from the seafloor into the seismogenic zone, *Geology,* **41,** 991–994.

Rowe, K.T., Screaton, E.J. & Ge, S., 2012. Coupled fluid flow and deformation modeling of the frontal thrust region of the Kumano Basin transect, Japan: implications for fluid pressures and decollement downstepping, *Geochem. Geophys. Geosyst.,* **13,** doi:10.1029/2011GC003861.

Saffer, D.M., 2003. Pore pressure development and progressive dewatering in underthrust sediments at the Costa Rican subduction margin: comparison with northern Barbados and Nankai, *J. geophys. Res.: Solid Earth (1978–2012),* **108,** doi:10.1029/2002JB001787.

Saffer, D.M. & Bekins, B.A., 1998. Episodic fluid flow in the Nankai accretionary complex: timescale, geochemistry, flow rates, and fluid budget, *J. geophys. Res.: Solid Earth (1978–2012),* **103,** 30 351–30 370.

Saffer, D.M. & Bekins, B.A., 2006. An evaluation of factors influencing pore pressure in accretionary complexes: implications for taper angle and wedge mechanics, *J. geophys. Res.: Solid Earth (1978–2012),* **111**, B04101, doi:10.1029/2005JB003990.

Saffer, D.M. & Kopf, A., 2006. Quantifying the source regions of observed pore water B and δ11B signatures at shallow depths in forearcs, *EOS, Trans. Am. geophys. Un.,* AGU.

Saffer, D.M. & Marone, C., 2003. Comparison of smectite-and illite-rich gouge frictional properties: application to the updip limit of the seismogenic zone along subduction megathrusts, *Earth planet. Sci. Lett.,* **215,** 219–235.

Saffer, D.M. & Tobin, H.J., 2011. Hydrogeology and mechanics of subduction zone forearcs: Fluid flow and pore pressure, *Ann. Rev. Earth planet. Sci.,* **39,** 157–186.

Saffer, D.M., Underwood, M.B. & McKiernan, A.W., 2008. Evaluation of factors controlling smectite transformation and fluid production in subduction zones: application to the Nankai Trough, *Island Arc,* **17,** 208–230.

Sample, J.C., 1996. Isotopic evidence from authigenic carbonates for rapid upward fluid flow in accretionary wedges, *Geology,* **24,** 897–900.

Screaton, E.J., Wuthrich, D.R. & Dreiss, S.J., 1990. Permeabilities, fluid pressures, and flow rates in the Barbados Ridge Complex, *J. geophys. Res.: Solid Earth (1978–2012),* **95,** 8997–9007.

Sibson, R.H., 1996. Structural permeability of fluid-driven fault-fracture meshes, *J. Struct. Geol.,* **18,** 1031–1043.

Sibson, R.H. & Rowland, J.V., 2003. Stress, fluid pressure and structural permeability in seismogenic crust, North Island, New Zealand, *Geophys. J. Int.,* **154,** 584–594.

Skarbek, R.M. & Saffer, D.M., 2009. Pore pressure development beneath the décollement at the Nankai subduction zone: implications for plate boundary fault strength and sediment dewatering, *J. geophys. Res.: Solid Earth (1978–2012),* **114,** doi:10.1029/2008JB006205.

Spinelli, G. & Harris, R., 2011. Thermal effects of hydrothermal circulation and seamount subduction: temperatures in the Nankai Trough Seismogenic Zone Experiment transect, Japan, *Geochem. Geophys. Geosyst.,* **12,** doi:10.1029/2011GC003727.

Spinelli, G.A., Saffer, D.M. & Underwood, M.B., 2006. Hydrogeologic responses to three-dimensional temperature variability, Costa Rica subduction margin, *J. geophys. Res.,* **111,** B04403, doi:10.1029/2004JB003436.

Tobin, H.J. & Kinoshita, M., 2006. NanTroSEIZE: the IODP Nankai Trough seismogenic zone experiment, *Sci. Drill,* **2,** 23–27.

Tobin, H.J. & Saffer, D.M., 2009. Elevated fluid pressure and extreme mechanical weakness of a plate boundary thrust, Nankai Trough subduction zone, *Geology,* **37,** 679–682.

Townend, J., 1997a. Subducting a sponge, *GSNZ Newslett.,* **112,** 14–16.

Townend, J., 1997b. Estimates of conductive heat flow through bottom-simulating reflectors on the Hikurangi and southwest Fiordland continental margins, New Zealand, *Mar. Geol.,* **141,** 209–220.

Wallace, L.M. & Beavan, J., 2010. Diverse slow slip behavior at the Hikurangi subduction margin, New Zealand, *J. geophys. Res.: Solid Earth (1978–2012),* **115,** doi:10.1029/2010JB007717.

Wallace, L.M. *et al.*, 2009. Characterizing the seismogenic zone of a major plate boundary subduction thrust: Hikurangi Margin, New Zealand, *Geochem. Geophys. Geosyst.,* **10,** doi:10.1029/2009GC002610.

Wallace, L.M., Beavan, J., McCaffrey, R. & Darby, D., 2004. Subduction zone coupling and tectonic block rotations in the North Island, New Zealand, *J. geophys. Res.: Solid Earth (1978–2012),* **109,** doi:10.1029/2004JB003241.

Wallace, L.M., Beavan, J., Bannister, S. & Williams, C., 2012. Simultaneous long-term and short-term slow slip events at the Hikurangi subduction margin, New Zealand: implications for processes that control slow slip event occurrence, duration, and migration, *J. geophys. Res.: Solid Earth (1978–2012),* **117,** doi:10.1029/2012JB009489.

Wang, K., 1994. Kinematic models of dewatering accretionary prisms, *J. geophys. Res.,* **99**(B3), 4429–4438.

Wang, K. & Bilek, S.L., 2014. Invited review paper: Fault creep caused by subduction of rough seafloor relief, *Tectonophysics,* **610,** 1–24.

You, C., Spivack, A., Gieskes, J., Rosenbauer, R. & Bischoff, J., 1995. Experimental study of boron geochemistry: implications for fluid processes in subduction zones, *Geochim. Cosmochim. Acta,* **59,** 2435–2442.

You, C.-F., Castillo, P., Gieskes, J., Chan, L. & Spivack, A., 1996. Trace element behavior in hydrothermal experiments: implications for fluid processes at shallow depths in subduction zones, *Earth planet. Sci. Lett.,* **140,** 41–52.

Zhao, Z., Moore, G.F. & Shipley, T.H., 1998. Deformation and dewatering of the subducting plate beneath the lower slope of the northern Barbados accretionary prism, *J. geophys. Res.,* **103**(B12), 30 431–30 449.

SUPPORTING INFORMATION

Additional Supporting Information may be found in the online version of this paper:

Figure ES1. (a) Velocity determined by high density velocity analysis derived from the multichannel seismic data along line 05CM-04 at $x = -35$ km (see Fig. 2 for location of this profile). The shaded regions represent the range of velocity functions and transformations derived for this site using two separate pre-stack depth migration velocity analyses. (b) Calculated density derived using the relationships of Brocher (2005) and Gardner *et al.* (1974). Red highlight of reference indicates method used in the main paper for fluid budget analysis. (c) Porosity calculations. The four porosity curves were derived using: Erickson & Jarrard (1998) using normal (NC) and high compaction (HC), Gardner *et al.* (1974) and Brocher (2005) (assuming a particle density of 2750 kg m^{-3}). Red highlight of reference indicates method used in the main paper. Note that the porosity varies more between transformation methods than from velocity variations alone, i.e. the blue shaded area (c), derived from the range of velocity values (a) using Erickson & Jarrard (1998) normal compaction gives less spread than the porosity values derived from the four different velocity-porosity relationships at depths greater than 4 km.

Figure ES2. Comparison between weak, moderate and strong fault friction (angles of friction 2°, 8.5° and 25°, respectively, and fluid pressure ratio of 0.65. Colour contours are velocity magnitude (0–50 mm yr^{-1}) and with velocity vectors at selected points superimposed. The strong detachment case predicts deformation all the way to the backstop, which is not consistent with preliminary structural reconstructions that suggest that most recent deformation has occurred in the frontal part of the wedge (between $x = -20$ and 0 km).

Figure ES3. The horizontal gradient in the porosity field of Fig. 2(b) (dn/dx).

Figure ES4. (a) Initial setup of numerical experiment with subducting seamount. Backstop (red), sediment (blue, yellow layers) and slab (white) have dry friction angles of 35°, 30° and 30°, respectively, while weak detachment has a dry friction angle of 8°. Hydrostatic fluid pressure is assumed, so that these correspond to effective friction coefficients of 20°, 17.5° and 4.8°, respectively. Cohesion is 1 MPa for all material except detachment where it is negligible. A boundary velocity of 5 cm yr^{-1} is applied along the right-hand edge of the model and at the base and below of the backstop parallel to the detachment layer. An initial taper of 1° is applied at the top of the model (which is a free surface). (b) Geometry after 1 Myr of deformation. The seamount has created, and then passed landward of, a steep frontal wedge. (c) Strain-rate invariant (colour contours) and velocity vectors after 1 Myr. (d) Nominal model from the main paper (Fig. 3), and equivalent for a higher detachment strength, using present-day geometry and inferred materials at depth for comparison. Dry friction angles along detachment labelled to left of panels are for a fluid pressure ratio $\lambda = 0.65$. (http://gji.oxfordjournals.org/lookup/suppl/doi:10.1093/gji/ggv127/-/DC1)

Please note: Oxford University Press is not responsible for the content or functionality of any supporting materials supplied by the authors. Any queries (other than missing material) should be directed to the corresponding author for the paper.